

# Geostatistical Earth Modeling of Cyclic Depositional Facies and Diagenesis

Thomas Le Blévec, Olivier Dubrule, Cédric M. John, Gary J. Hampson

February 19, 2019

1 Thomas Le Blévec

2 t.le-blevec15@imperial.ac.uk

3 Earth Science and Engineering, Imperial College, London, UK

4 Olivier Dubrule

5 o.dubrule@imperial.ac.uk

6 Earth Science and Engineering, Imperial College, London, UK

7 Cédric M. John

8 cedric.john@imperial.ac.uk

9 Earth Science and Engineering, Imperial College, London, UK

10 Gary J. Hampson

11 g.j.hampson@imperial.ac.uk

12 Earth Science and Engineering, Imperial College, London, UK

## 13 **Acknowledgements**

14 The authors would like to thank Carl Jacquemyn and Claire Veillard for providing  
15 practical examples and contributing ideas to this paper, and the department of Earth  
16 Science and Engineering at Imperial College for Thomas Le Blévec's scholarship.  
17 Olivier Dubrule would like to thank Total for seconding him at Imperial College  
18 London.

## 19 Abstract

20 In siliciclastic and carbonate reservoirs, depositional facies are often described as be-  
21 ing organized in cyclic successions that are overprinted by diagenesis. Most reservoir  
22 modeling workflows are not able to reproduce stochastically such patterns. Herein,  
23 a novel geostatistical method is developed to model depositional facies architectures  
24 that are rhythmic and cyclic, together with superimposed diagenetic facies.

25 The method uses truncated Pluri-Gaussian random functions constrained by  
26 transiograms. Cyclicity is defined as an asymmetric ordering between facies, and  
27 its direction is given by a three-dimensional vector, called shift. This method is  
28 illustrated on two case studies. Outcrop data of the Triassic Latemar carbonate  
29 platform, northern Italy, are used to model shallowing-upward facies cycles in the  
30 vertical direction. A satellite image of the modern Bermuda platform interior is used  
31 to model facies cycles in the windward-to-leeward lateral direction.

32 As depositional facies architectures are modeled using two Gaussian random  
33 functions, a third Gaussian random function is added to model diagenesis. Thereby,  
34 depositional and diagenetic facies can exhibit spatial asymmetric relationships. The  
35 method is applied in the Latemar carbonate platform that experiences syn-depositional  
36 dolomite formation. The method can also incorporate proportion curves to model  
37 non-stationary facies proportions. This is illustrated in Cretaceous shallow-marine  
38 sandstones and mudstones, Book Cliffs, Utah, for which cyclic facies and diagenetic  
39 patterns are constrained by embedded transition probabilities.

## 40 Introduction

41 In reservoir modeling applications, an important step is the representation of three-  
42 dimensional facies architecture and the quantification of associated uncertainty. The  
43 geomodeling community routinely uses geostatistical methods to reach this goal  
44 (Koltermann and Gorelick, 1996; Alabert and Modot, 1992; Pyrcz and Deutsch,  
45 2014). However, the commonly-used geostatistical approaches have some signif-

46 icant limitations. For instance, geostatistical models often show the same facies  
47 successions in the upward as in the downward direction, which does not allow the  
48 representation of classic geological features such as facies cyclicity or certain types  
49 of syn-depositional diagenesis.

## 50 **Modeling Cyclicity and Rhythmicity**

51 Depositional facies in vertical successions exhibit extensive cyclicity and rhythmic-  
52 ity (Strasser, 1988; Goldhammer et al., 1990; Wilkinson et al., 1997; Lindsay et al.,  
53 2006; Burgess, 2016). These features are defined respectively as facies ordering (Gin-  
54 gerich, 1969; Hattori, 1976) and repetition of facies at intervals of constant thickness  
55 (De Boer and Wonders, 1984; House, 1985). Their origin is attributed to various  
56 controls, including relative sea level oscillations (e.g., Grotzinger, 1986), local tec-  
57 tonic activity (e.g., Cisne, 1986) and autogenic mechanisms. These different origins  
58 may lead to cycles and rhythms of differing lateral extent and stacking patterns,  
59 which should be reproduced by the modeling method. For example, facies cycles  
60 are commonly interpreted at reservoir scale with reference to sequence stratigraphic  
61 models, implying that they are laterally extensive (e.g., Goldhammer et al., 1990),  
62 although over such distances, some facies cycles are documented to pinch out (e.g.,  
63 Egenhoff et al., 1999). In order to represent these diverse facies cycles and rhythms,  
64 reservoir-wide deterministic correlations may not be appropriate.

65 Diverse facies distributions are modeled by geostatistical methods, but their cur-  
66 rent implementation cannot generate facies cycles and rhythms simultaneously. For  
67 example, cyclicity quantification is possible with Markov Chain analysis (Gingerich,  
68 1969; Hattori, 1976), but the method is originally limited to one dimension. It was  
69 later improved by Carle and Fogg (1996, 1997) who model cyclic three dimensional  
70 Earth models thanks to asymmetric transiograms. However, the method does not  
71 incorporate rhythmicity, because the transiogram models are not flexible enough to  
72 incorporate the characteristic periodic oscillations (Jones and Ma, 2001; Dubrule,  
73 2017), called hole-effects. Facies cyclicity and rhythmicity could theoretically be

74 modeled by multi-point statistics (Strebelle, 2002), but it is challenging to include  
75 those patterns in the required three dimensional training image.

76 A geostatistical method has been developed recently to model simultaneously  
77 facies cyclicity and rhythmicity (Le Blévec et al., 2018), thus improving the real-  
78 ism of facies Earth models. The method is based on Pluri-Gaussian Simulations  
79 (Armstrong et al., 2011), constrained by facies transiograms. The facies asymmetric  
80 ordering (or cyclicity) is defined by two Gaussian random functions spatially shifted  
81 from each other, and rhythmicity of the facies succession is modeled by defining  
82 new hole-effect covariance models (Le Blévec et al., 2018). However, the method  
83 has only be tested so far for a model with three facies and it might be more difficult  
84 to model cyclicity with more facies, which is investigated here.

85 Moreover, this method has only been used to model cyclicity in the vertical  
86 direction, although cyclicity can also be observed in lateral directions. Stratigraphic  
87 forward models can produce asymmetry between facies in lateral directions (Burgess  
88 et al., 2001), and such lateral facies asymmetry is also explicit within Walther’s Law  
89 (e.g., Middleton, 1973). This could possibly be modeled with the shifted Pluri-  
90 Gaussian method (Le Blévec et al., 2018) by defining a spatial shift with a lateral  
91 component.

## 92 **Modeling Diagenesis**

93 Reservoir quality is not only affected by depositional facies cyclicity. Rock properties  
94 of carbonate (e.g., Bartok et al., 1981; Moore and Wade, 2013) and siliciclastic (e.g.,  
95 Taylor et al., 2010) deposits are also influenced by diagenesis. Diagenetic processes  
96 give rise to depositional and diagenetic facies with a variety of geometrical relation-  
97 ships, which should be captured by the modeling method. Early diagenesis tends to  
98 closely follow the texture and stratal configuration of depositional facies (e.g., Gins-  
99 burg, 1957; Egenhoff et al., 1999; Peterhänsel and Egenhoff, 2008; Rameil, 2008)  
100 while late diagenesis either follow depositional features, or other structures such as  
101 faults, fractures, and karsts, thus resulting in diagenetic bodies and trends that cut

102 across depositional facies geometries (e.g., [Sharp et al., 2010](#); [Vandeginste et al.,](#)  
103 [2013](#); [Jacquemyn et al., 2014](#); [Beckert et al., 2015](#)). It is, therefore, highly desir-  
104 able that reservoir modeling methods are flexible enough to embrace these different  
105 possibilities.

106 In many geostatistical studies, diagenesis is modeled as porosity or permeability  
107 variations ([Wang et al., 1998](#); [Pontiggia et al., 2010](#)). This is a useful approach,  
108 but it cannot be applied to the representation of distinct diagenetic geobodies or  
109 of different diagenetic phases within a depositional facies. Therefore, some authors  
110 model diagenesis as a facies random field that is superimposed on the depositional  
111 facies field ([Renard et al., 2008](#); [Doligez et al., 2011](#); [Barbier et al., 2012](#); [Carrera](#)  
112 [et al., 2018](#)). These authors use a version of truncated Pluri-Gaussian Simulations  
113 (Bi-PGS) developed by [Renard et al. \(2008\)](#), which models two facies fields with  
114 different Gaussian random functions. The depositional and diagenetic facies fields  
115 can be either independent of or correlated to each other, which allows the modeling  
116 of depositional and diagenetic facies geometries that are either discordant or con-  
117 formable. However, this method does not generate distributions of diagenetic facies  
118 that are asymmetric such as occurring preferentially towards the top or the base of  
119 depositional facies bodies.

120 The algorithm of [Renard et al. \(2008\)](#) to model diagenesis is thus extended  
121 here by including a shift between depositional and diagenetic facies fields, which  
122 allows diagenetic facies to overprint depositional facies preferentially at their top or  
123 at their base. These relationships are constrained by cross-transiograms between  
124 the two facies fields, and the method is also combined with the advancements of  
125 [Le Blévec et al. \(2018\)](#), so that diagenesis is modeled in the context of depositional  
126 facies cyclicity and rhythmicity.

## 127 **Aims**

128 This paper presents a new geostatistical facies modeling method that is able to rep-  
129 resent facies cyclicity and rhythmicity, together with diagenetic facies bodies. The

130 structure of the paper is outlined below. First, the paper illustrates the concepts of  
131 cyclicity and rhythmicity and it is shown that these concepts are captured by tran-  
132 siograms. Modeling of cycles and rhythms is then illustrated using: (1) synthetic  
133 facies successions; (2) facies successions from the outcropping Triassic Latemar car-  
134 bonate platform of northern Italy; and (3) lateral facies relationships on the interior  
135 of the modern Bermuda carbonate platform. Then, diagenesis is modeled by adding  
136 another Gaussian random function to the method. Two examples are modeled to  
137 illustrate the flexibility of the method: (1) syn-depositional diagenesis below hard-  
138 grounds in facies cycles of the Latemar carbonate platform; and (2) early diagenetic  
139 development of concretions in shallow-marine, siliciclastic facies cycles in the Cre-  
140 taceous Blackhawk Formation, Book Cliffs outcrops (Utah), in which the facies  
141 proportions are non-stationary.

## 142 **Quantifying Cyclicity and Rhythmicity with Tran-** 143 **siograms**

### 144 **Defining Cyclicity and Rhythmicity**

145 Although facies cyclicity and rhythmicity are commonly interpreted in sedimentary  
146 sequences, these concepts have different meanings to different authors. Formal,  
147 quantitative definitions of cyclicity and rhythmicity are needed for facies modeling,  
148 as a facies succession can be more or less ordered or exhibit more or less variability in  
149 facies thickness. Cyclicity is defined as facies ordering in a given direction ([Gingerich,](#)  
150 [1969](#); [Hattori, 1976](#); [Le Blévec et al., 2018](#)), usually vertically (Fig. 1). The ordering  
151 considered here is asymmetric, which means that it differs going upwards from going  
152 downwards. For instance, in vertical shallow-marine carbonate and siliciclastic suc-  
153 cessions, facies cycles tend to be shallowing-upward ([Strasser, 1988](#); [Goldhammer](#)  
154 [et al., 1990](#); [Lindsay et al., 2006](#)), which is equivalent to deepening-downward.

155 Another commonly observed feature is that the same facies tends to appear re-

156 peatedly at intervals of constant thickness (e.g., Goldhammer et al., 1993; Lindsay  
157 et al., 2006), which defines rhythmicity (De Boer and Wonders, 1984; House, 1985;  
158 Le Blévec et al., 2018). If cyclicity and rhythmicity are both present, it implies  
159 that the facies cycles have low variability in thickness. For instance, the vertical  
160 succession in Figure 1a is cyclic and rhythmic because the facies are fully ordered  
161 and have constant thickness intervals between them. The succession illustrated in  
162 Figure 1b has non-ordered transitions between facies and also contains two facies  
163 cycles. The succession in Figure 1c also contains two facies cycles, and the blue  
164 facies is rhythmic, because intervals between occurrences of this facies have similar  
165 thickness. Figure 1d shows a cyclic and non-rhythmic facies succession, and the suc-  
166 cession in Figure 1a is cyclic and rhythmic, because the facies are fully ordered and  
167 the blue facies is separated by intervals of constant thickness. For three-dimensional  
168 Earth models to be geologically realistic, facies cyclicity and rhythmicity must be  
169 properly modeled.

## 170 **The Transiogram: a Tool to Capture Cyclicity and Rhythmic-** 171 **ity**

172 Standard geostatistical simulation approaches quantify geologic patterns by comput-  
173 ing experimental variograms, modeling them mathematically and then ensuring that  
174 the variogram models are reproduced in the final simulation (Pyrcz and Deutsch,  
175 2014). However, Carle and Fogg (1996) show that variograms are not able to quan-  
176 tify asymmetric cycles, and promote the use of the transiogram instead.

177 The transiogram gives the probability  $t_{AB}(h)$  of finding a facies  $B$  at a vector  
178  $h$  from a given facies  $A$  (Carle and Fogg, 1996; Le Blévec et al., 2018). If the two  
179 facies  $A$  and  $B$  are identical, the transiogram is referred to as an auto-transiogram,  
180 otherwise it is referred to as a cross-transiogram. Auto-transiograms and cross-  
181 transiograms are calculated experimentally and gathered in a transiogram matrix  
182 (Fig. 2). As with variograms, the direction  $h$  is usually vertical, but it can also have  
183 a lateral component if calculated along other directions. For sedimentary facies,

184 cross-transiograms are commonly different in opposite directions (e.g., upward and  
185 downward) (Carle and Fogg, 1996).

186 Transiograms have specific properties, which are described in detail by Carle and  
187 Fogg (1996). One property is that at long distances  $h$ ,  $t_{AB}(h)$  tends towards the  
188 proportion of facies  $B$ . For example, Figure 2b-e shows that the transiograms tend  
189 towards the value of 0.5, which is the proportion of facies 1, and 0.25, which is the  
190 proportion of facies 2. Also, the tangent at the origin  $t'_{AA}(0)$  of the auto-transiogram  
191  $t_{AA}(h)$  defines the mean length of facies  $A$  in the direction of  $h$ , denoted as  $\overline{L}_A$  (Carle  
192 and Fogg, 1996), as shown in Figure 2b, e ( $\overline{L}_1$  and  $\overline{L}_2$ ).

193 Figure 2c, and 2d also show that cyclicity is captured by the behavior at the  
194 origin of the cross-transiograms (Le Blévec et al., 2018).  $t'_{12}(0)$  is high while  $t'_{21}(0)$  is  
195 low, which means that facies 2 tends to overlie facies 1, while facies 1 does not tend  
196 to overlie facies 2. Consequently facies 3 overlies facies 2, creating facies cycles with  
197 facies 1 at the base, facies 2 in the center and facies 3 at the top. This cyclicity is  
198 observed in the corresponding succession (Fig. 2a), which shows that facies 1 almost  
199 always transitions upward to facies 2 (except on one occasion when it transitions  
200 directly to facies 3), and facies 2 transitions upward to facies 3.

201 Rhythmicity is characterized by the oscillations of the transiograms or variograms  
202 (Jones and Ma, 2001; Le Blévec et al., 2018), as shown in Figure 2. The average  
203 distance separating two repetitions of a facies is given by the first maximum of the  
204 corresponding auto-transiogram, as this is associated with the highest probability  
205 of finding the same facies (Fig. 2b, e,  $\overline{L}_c = 0.4$  m ( $\sim 1.3$  ft)). It also corresponds to  
206 the first minimum of the cross-transiograms (Fig. 2c, d), which is associated with  
207 the lowest probability of finding two different facies. In this case, because there  
208 is also cyclicity, this length  $\overline{L}_c$  corresponds to the average thickness of the facies  
209 cycle and is approximately the sum of the mean thicknesses of all facies present in  
210 a cycle. This also explains why the auto-transiogram of facies 2 shows the same  
211 rhythmicity (Fig. 2e) as the auto-transiogram of facies 1 (Fig. 2b). Rhythmicity can  
212 be visually verified by examining the corresponding succession (Fig. 2a), which shows



213 that facies cycles indeed exhibit low thickness variations (thickness of approximately  
214 0.4 m ( $\sim 1.3$  ft)). Therefore, transiograms appear to be better suited than variograms  
215 to the quantification of cyclicity and rhythmicity.

## 216 Modeling Cyclicity and Rhythmicity with Shifted Pluri- 217 Gaussian Simulations

### 218 Principle of Truncated Gaussian Simulations

219 The truncated Gaussian approach for facies modeling was first developed by [Math-](#)  
220 [eron et al. \(1988\)](#) and is explained in detail by [Armstrong et al. \(2011\)](#). It has  
221 two steps: (1) first, the simulation of a continuous Gaussian random function, and  
222 then (2) the truncation of this continuous function into facies with the help of a  
223 truncation rule.

224 A Gaussian random function defines at every location  $(x, y, z)$  (usually in a  
225 grid) a Gaussian random variable. The Gaussian random function is controlled by  
226 its covariance model ([Chiles and Delfiner, 2012](#)). In this paper, as explained in  
227 the Appendix, Gaussian cosine covariances (with frequency parameter  $b$ ) are used  
228 with scale factor noted  $r_z$  (Eq. [A.4a](#)) in the vertical direction. In lateral directions  
229 Gaussian covariances are used, with scale factors noted  $r_x$  and  $r_y$  for each principal  
230 direction (Eq. [A.4a](#)). Scale factors control the average length scale of the Gaussian  
231 random functions in the corresponding direction and  $b$  their periodicity ([Le Blévec](#)  
232 [et al., 2018](#)). Figure [3a](#) (red curve) shows an example of a realization of a Gaussian  
233 random function  $Z_1$  along a vertical succession (i.e., on a one-dimensional grid).

234 The truncation rule defines the number of facies, their proportions, and their  
235 contacts. For instance, Figure [3b](#) shows a truncation rule with three facies, with  
236 a small area for facies 3 defined by the threshold  $q_2$ . This results in a smaller  
237 proportion of facies 3 in the corresponding vertical succession (Fig. [3a](#)). As shown  
238 by Figure [3a](#), when  $Z_1$  is higher than  $q_1$ , facies 2 is allocated, and when it reaches

239  $q_2$ , facies 3 is defined.

240 By using only one Gaussian random function, modeling is limited because each  
241 facies can only transition into one or, at most two other facies. For instance, in  
242 Figure 3, facies 1 and 3 can only transition into facies 2, while facies 2 can transition  
243 into both facies 1 and 2 upward or downward. Therefore, cyclicity cannot be modeled  
244 because there is no asymmetry associated with the simulation. [Armstrong et al.](#)  
245 (2011) extend the method to Pluri-Gaussian Simulations, and it was then modified  
246 by [Le Blévec et al. \(2018\)](#) to model cyclicity.

## 247 The Shifted Pluri-Gaussian Simulations Approach

248 This section summarizes the modeling method developed in [Le Blévec et al. \(2018\)](#).  
249 The method is based on Pluri-Gaussian Simulations (PGS) ([Armstrong et al., 2011](#)),  
250 which generalizes Truncated Gaussian Simulations by using several Gaussian ran-  
251 dom functions instead of just one. An example is given in Figure 4b, which shows  
252 a Pluri-Gaussian Simulation using two Gaussian random functions  $Z_1$  and  $Z_2$ . The  
253 variations of each Gaussian random function are controlled by their respective co-  
254 variance model (Eqs. [A.4a](#) and [A.4b](#)). The truncation rule applied to them is two  
255 dimensional (Fig. 4a) and defines in this example three facies by two thresholds  $q_1$   
256 and  $q_2$ , with all three facies in contact with each other. For instance, the defined  
257 facies is yellow if  $q_1$  is smaller than  $Z_1$  and  $q_2$  is smaller than  $Z_2$ . The corresponding  
258 facies succession (Fig. 4b) shows no specific cyclicity, because all facies can transition  
259 into each other randomly.

260 In order to model cyclicity, [Le Blévec et al. \(2018\)](#) introduced a spatial shift  
261  $\alpha$  between the two Gaussian random functions. More specifically, the Gaussian  
262 random functions are correlated (or anti-correlated) to each other by a correlation  
263 coefficient  $\beta$ , then shifted by a vector noted  $\alpha$  (Eq. [A.3](#)), which gives the direction  
264 of the cyclicity. This is illustrated in Figure 4c, in which the Gaussian random  
265 functions are anti-correlated ( $\beta < 0$ ), with a small shift  $\alpha$  oriented upward. This  
266 results, after truncation, into a highly cyclic facies succession (Fig. 4c). The upward

267 cycle from facies 1 to facies 2 then to facies 3 is repeated almost everywhere because  
268  $Z_2$  tends to cross its threshold  $q_2$  (from facies 2 to facies 3) just after  $Z_1$  crosses its  
269 threshold  $q_1$  (from facies 1 to facies 2), as if the truncation rule (Fig. 4a) had an  
270 anti-clockwise motion in the upward direction. The cyclicity of the succession shown  
271 in Figure 4c is confirmed by its corresponding transiograms (Fig. 2) as explained  
272 previously.

## 273 Modeling Vertical Facies Cyclicity and Rhythmicity in the 274 Latemar Carbonate Platform

### 275 Dataset

276 The Triassic Latemar carbonate platform (northern Italy) is renowned for its cyclic-  
277 ity (Goldhammer et al., 1990; Hinnov and Goldhammer, 1991) and is thus well suited  
278 for analysis by the new method described above. Using the original data of Peter-  
279 hänsel and Egenhoff (2008), part of the Upper Cyclic Facies interval has previously  
280 been modeled by Le Blévec et al. (2018) with a simplified, three-fold classification  
281 of depositional facies that is modified from Egenhoff et al. (1999). Here, the same  
282 interval is modeled in the Cimon Latemar outcrop with the full four-fold classifi-  
283 cation of depositional facies of Egenhoff et al. (1999): subtidal ( $e_1$ ), intertidal ( $e_2$ ),  
284 supratidal ( $e_3$ ) and subaerial exposure facies ( $e_4$ ). Diagenetic overprinting is at first  
285 not considered in the model described here, but models of the Latemar platform  
286 presented later include diagenetic facies. Although depositional facies are here de-  
287 nominated as environments of deposition, their interpretation is directly based on  
288 application of the Dunham classification to observations in thin sections (Egenhoff  
289 et al., 1999). Therefore, it is possible that they transition laterally with each other  
290 several times at the same stratigraphic level, in a mosaic-like fashion, as shown by  
291 the interpreted cross section of Peterhänsel and Egenhoff (2008). The measured  
292 sections and the interpreted cross section of Peterhänsel and Egenhoff (2008) are  
293 presented in Figure 5 and Figure 8a.

294 As discussed by Egenhoff et al. (1999) and Peterhänsel and Egenhoff (2008), the

295 facies tend to be organized in shallowing-upward facies cycles that comprise, from  
296 base to top, facies  $e_1$ , facies  $e_2$ , facies  $e_3$ , facies  $e_4$ . This interpreted organization is  
297 supported by logs in Figure 5. For example, the subtidal facies  $e_1$  tends to overlies  
298 the subaerial exposure facies  $e_4$ , which defines the base of a cycle, and is generally  
299 overlain by intertidal facies  $e_2$ . However, many cycles are incomplete and lack one or  
300 more facies (Fig. 5). There is also a high number of alternations between intertidal  
301 facies  $e_2$  and subaerial exposure facies  $e_4$  (e.g., in log N17, Fig. 5). Therefore, the  
302 cyclicity of the facies succession is not perfect and this imperfect pattern should be  
303 reproduced statistically in the model. It is also noteworthy that subtidal facies  $e_1$   
304 and supratidal facies  $e_3$  are never in contact (Fig. 5).

## 305 Model

306 The first step is to define an appropriate truncation rule based on the observed  
307 contacts between facies and their cyclicity. As the typical cycle is  $e_1 \rightarrow e_2 \rightarrow e_3 \rightarrow$   
308  $e_4$ , these facies should be arranged clockwise (or counter-clockwise) in the truncation  
309 rule. Moreover, as observed (Fig. 5), subtidal facies should not be in contact with  
310 supratidal facies. Figure 6 shows a truncation rule satisfying these constraints.

311 The next step is to find the parameters of the model ( $\beta_{12}$ ,  $\alpha_{12}$ ,  $r_1$ ,  $r_2$ ,  $b_1$ ,  $b_2$ ) from  
312 the experimental transiograms computed from the logs. A trial-and-error test is  
313 performed on the parameters, and the ones that give the best fit between experi-  
314 mental and theoretical transiograms are chosen. For each trial of these parameters,  
315 the thresholds  $q_1$ ,  $q_2$  and  $q_3$  are computed in order to match the proportions of the  
316 different facies (an example of how to compute the thresholds from the proportions  
317 is given in the Appendix, using Eqs. A.7, A.8 and A.9). The computation of a theo-  
318 retical transiogram from the parameters of the method is explained in the Appendix  
319 (Eqs. A.10, A.11 and A.12). The results are shown in Figure 7 (grey points).

320 It is important to note that transiograms are inter-dependent and cannot be fitted  
321 individually. For instance, the first maximum of the auto-transiograms and first  
322 minimum of the cross-transiograms are related to the cycle thickness, as explained

323 earlier (Fig. 2). Thus, one parameter such as the shift  $\alpha_{12}$  controls the behavior of  
324 several theoretical transiograms (see [Le Blévec et al., 2017](#), for details). Because  
325 of these relationships between transiograms, it is usually not possible to obtain a  
326 perfect fit between experimental and theoretical transiograms, and a compromise  
327 should be made based on which feature (or combination of features) is considered  
328 by the user to be more important.

329 The theoretical transiograms after fitting are shown in Figure 7 (black curves).  
330 The tangents at the origin of the different auto-transiograms and cross-transiograms  
331 are matched, which means that the different facies thicknesses and the contacts  
332 between them are well constrained. Therefore, the fit between experimental and  
333 theoretical transiograms is satisfactory. Subtidal facies  $e_1$  and supratidal facies  $e_3$   
334 are not in contact because  $t_{e_1e_3}(h)$  and  $t_{e_3e_1}(h)$  both have a tangent at the origin  
335 with a very low value, which comes from the truncation rule (Fig. 6). The only  
336 significant mismatch is for the cross-transiogram  $t_{e_4e_1}(h)$ , for which the tangent at  
337 the origin of the theoretical transiogram is not high enough (Fig. 7). This means  
338 that in the model, facies  $e_1$  has less tendency to overlie facies  $e_4$  than in the dataset.

339 Some rhythmic facies patterns are also captured, such as the one observed in the  
340 transiogram  $t_{e_1e_1}(h)$  (Fig. 7).

341 The scale factors in the lateral direction  $r_x$  and  $r_y$  are chosen by visual comparison  
342 of the resulting facies models with the outcrop cross section of [Peterhänsel and](#)  
343 [Egenhoff \(2008\)](#). The higher their values, the larger the extent of the facies. As the  
344 facies are quite laterally extensive, the scale factors are of the order of the size of  
345 the final Earth model of depositional facies.

## 346 **Simulation**

347 The Earth model for depositional facies is now built using the above fitted parame-  
348 ters. The Gaussian random functions are simulated in the grid described below, and  
349 then truncated into facies. The simulations are also conditioned to the measured  
350 sections so that the facies observed in the measured sections are reproduced in the

351 model realizations. The algorithms to perform these steps are explained in [Le Blévec](#)  
352 [et al. \(2018\)](#).

353 The number of grid cells in each direction (East, North, Z) is (100, 10, 182), and  
354 the grid dimensions are (1000 m, 250 m, 9.1 m)~(0.62 mi, 820 ft, 29 ft). Hence the  
355 size of each cell is (10 m, 25 m, 5 cm)~(33 ft, 82 ft, 0.16 ft). The number of cells is  
356 a compromise between the desired computational speed of the simulation and the  
357 level of details at which the heterogeneities are represented. Here, a high resolution  
358 is chosen in the vertical direction, because most of the transitions between facies are  
359 vertical. The simulation is fast and several equiprobable realizations are obtained  
360 in two or three minutes with a standard desktop PC. Two realizations are shown  
361 in Figure 8b and c, together with the original measured sections of [Peterhänsel and](#)  
362 [Egenhoff \(2008\)](#), reproduced in both realizations.

363 Incomplete facies cyclicity, as observed in the measured sections (Fig. 5) is visible  
364 in the realizations (Fig. 8). For instance, subaerial exposure facies  $e_4$  are not only  
365 overlain by subtidal facies  $e_1$  at the base of each cycle, but also by intertidal facies  $e_2$   
366 or supratidal facies  $e_3$ . Subtidal facies  $e_1$  and supratidal facies  $e_3$  are not in contact,  
367 as defined by the truncation rule (Fig. 6). Laterally, facies transition randomly  
368 into each other because no lateral transition constraint is given. This aspect of the  
369 Earth model realizations can be improved by using conceptual knowledge of the  
370 platform-interior facies architecture, leading to Earth models that exhibit lateral  
371 facies cyclicity or non-stationarity, as illustrated below.

372 For model validation, the transiograms are computed in three realizations of  
373 the simulation and shown in Figure 7 (thin grey curves). Most transiograms of  
374 the realizations are a good fit to the experimental and theoretical transiograms,  
375 which shows that the Earth models are geologically realistic. Some mismatches also  
376 appear, for instance in  $t_{e_2e_2}(h)$ , for which it seems that the realizations have a higher  
377 plateau than the model. However, these statistical variations are not systematic and  
378 are common with stochastic simulations ([Chiles and Delfiner, 2012](#)).

## 379 Extension to Lateral Cyclicity

380 Lateral facies cyclicity can be observed in modern environments or generated by  
381 forward stratigraphic modeling (Burgess et al., 2001). Tidal-flat and reef islands  
382 deposits in modern shallow-water carbonate environments can exhibit lateral di-  
383 rectionality, induced by currents in the water column, which results in lateral and  
384 vertical facies cyclicity (e.g., Burgess et al., 2001). The method developed here mod-  
385 els such vertical and lateral facies cyclicity by adding a lateral component to the  
386 shift  $\alpha$  between the Gaussian random functions. This procedure is demonstrated  
387 using a satellite image of reef islands in the interior of the modern Bermuda plat-  
388 form, which was first described by Verrill (1907) (Fig. 9a). The reef island deposits  
389 show a lateral facies asymmetry, with a typical facies cycle comprising reef, backreef,  
390 and lagoonal facies (after Jordan Jr, 1973). Although there are no data describing  
391 the vertical facies succession, it is assumed that Walther’s law (Middleton, 1973) is  
392 followed, such that the lateral facies transitions are equivalent to the vertical facies  
393 transitions. This equivalence is modeled by incorporating the lateral component  
394 into the shift vector.

395 One unconditional (no vertical sections are matched) realization of an Earth  
396 model for facies distribution is shown in Figure 9c, along with the model truncation  
397 rule (Fig. 9b). The three modeled facies are in contact, and lateral facies cyclicity  
398 similar to that observed in the satellite image is generated. The vertical cyclicity is  
399 such that reef facies overlie backreef facies (Fig. 9c). The combination of lateral and  
400 vertical facies cyclicity results in an overall eastward progradation of reef islands.  
401 Therefore, the shift controls the movement over time of the facies belts and bodies.  
402 For instance, if the shift was oriented to the west, then this would be the direction  
403 of progradation. If the shift was purely vertical, there would only be aggradation.  
404 Due to the lateral component of the shift, Walther’s Law is respected in the model.

## 405 **Modeling Diagenesis with Shifted Pluri-Gaussian Sim-** 406 **ulations**

407 Siliciclastic and, particularly, carbonate reservoirs are widely documented to un-  
408 dergo extensive diagenetic modification during deposition and subsequent burial,  
409 which modifies their petrophysical properties (e.g., [Fabricius et al., 2007](#); [Makhloufi](#)  
410 [et al., 2013](#)). Therefore, it is important to provide a flexible modeling method for  
411 diagenetic overprinting of depositional facies that can mimic patterns resulting from  
412 multiple diagenetic events, in order to capture the impact on hydrocarbon recovery.  
413 Diagenesis can follow the original depositional fabric in some cases, resulting in spe-  
414 cific ordering between depositional and diagenetic facies. A novel method able to  
415 model such pattern is presented. By adding a third Gaussian function that controls  
416 diagenetic facies, the method co-simulates a depositional facies field and a diagenetic  
417 facies field. The shifts between the three Gaussian random functions allow the user  
418 to model asymmetric relationships between diagenetic and depositional facies.

## 419 **Modeling Syn-Depositional Diagenesis: Revisiting the Latemar** 420 **Carbonate Platform**

### 421 **Syn-Depositional Diagenesis in the Latemar Platform**

422 Previously, the Latemar carbonate platform was modeled using the measured sec-  
423 tions of [Peterhänsel and Egenhoff \(2008\)](#) as input data with depositional facies.  
424 However, the studies of [Egenhoff et al. \(1999\)](#) and [Peterhänsel and Egenhoff \(2008\)](#)  
425 also show that diagenesis affect these facies. Tepee structures, dolomitization and  
426 caliche crusts suggest an early diagenetic overprinting.

427 The measured sections of [Peterhänsel and Egenhoff \(2008\)](#) (Fig. 10) are again  
428 chosen as data for the model and their interpreted cross section (Fig. 14a) is used  
429 to control the lateral extent of the facies. These sections show two diagenetic facies:  
430 completely dolomitized crusts and partial dolomitization, which overprint different



431 depositional facies (Fig. 10). The dolomitic crust diagenetic facies only occurs in con-  
432 junction with subaerial exposure depositional facies, while the partially dolomitized  
433 diagenetic facies occurs in conjunction with intertidal and (marginally) supratidal  
434 depositional facies. This observation from vertical measured sections is supported  
435 by the interpreted lateral correlations of Peterhänsel and Egenhoff (2008) (Fig. 14a),  
436 in which the dolomitic crust diagenetic facies transitions laterally only into subaerial  
437 exposure depositional facies. Table 1 shows the proportions of each diagenetic facies  
438 within each depositional facies.

### 439 Model

440 In the Earth model realizations shown in Figure 8b and c, depositional facies were  
441 modeled using two Gaussian random functions. If diagenetic facies were included  
442 in the corresponding two dimensional truncation rule (Fig. 6), they would neces-  
443 sarily have geometric properties similar to those of depositional facies. Adding a  
444 third Gaussian random function as a third dimension in the truncation rule gives  
445 a greater flexibility to represent diagenetic facies geometries and their relationships  
446 with depositional facies. Moreover, diagenesis can then be modeled as a superim-  
447 posed facies field that overprints the depositional facies as explained in Renard et al.  
448 (2008). Adding more Gaussian random functions is also proposed in Madani and  
449 Emery (2015), but not in the context of diagenesis.

450 A three dimensional truncation rule for the Latemar platform is thus defined in  
451 Figure 11. The truncation rule for the depositional facies is the same as that shown  
452 in Figure 6. The third Gaussian random function defines two diagenetic facies:  
453 dolomitic crust  $d_1$  (which overprints subaerial exposure depositional facies  $e_4$ ) and  
454 partial dolomite  $d_2$  (which overprints intertidal and supratidal depositional facies  $e_2$   
455 and  $e_3$ ). Depositional facies  $e_1$  is not affected by diagenesis. The thresholds  $q$  con-  
456 trolling the proportions of diagenetic facies within depositional facies are computed  
457 from Table 1, as explained in the Appendix (Eq. A.7). For example, diagenetic  
458 facies  $d_2$  is more abundant in depositional facies  $e_2$  than in depositional facies  $e_3$ ,

459 and so its area is larger in the truncation rule (Fig. 11).

460 Once the truncation rule is chosen, the experimental transiograms of diagenetic  
461 facies are fitted with the parameters of the method, as described previously. Cross-  
462 transiograms between depositional and diagenetic facies are fitted first, because they  
463 are controlled by a smaller number of parameters:  $\alpha_{13}$ ,  $\beta_{13}$ ,  $\alpha_{23}$  and  $\beta_{23}$  (Eq. A.3).  
464 These parameters define the relations of the first two Gaussian random functions  
465  $Z_1$  and  $Z_2$  with the third Gaussian random function  $Z_3$  and thus control relation-  
466 ships between depositional facies and diagenetic facies. These cross-transiograms  
467 have different properties from usual cross-transiograms because they relate to two  
468 superimposed facies fields, for which facies can both be present at the same location.  
469 Therefore, their value at a distance  $h = 0$  is not 0 but the probability of finding  
470 the two facies types at the same location (Table 1). The fit between theoretical  
471 transiograms (black curves, Eq. A.11) and experimental transiograms (grey points)  
472 of depositional facies and diagenetic facies is shown in Figure 12.

473 For most transiograms, the experimental curve at the first distance step is com-  
474 monly higher than the theoretical curve (Fig. 12). This is due to the small number  
475 of data points, because there are few occurrences of diagenetic facies in the mea-  
476 sured sections (Fig. 10), thus causing the transiograms to be statistically unreliable.  
477 However, it is worth noting that the theoretical transiograms generally show reason-  
478 able behaviors at the origin. For instance, the tangent at the origin of transiogram  
479  $t_{d_1e_1}(h)$  has a high value (Fig. 12), which shows that subtidal depositional facies  
480 tends to overlie dolomitic crust diagenetic facies, as observed in the measured sec-  
481 tions (Fig. 10). This spatial relationship supports the facies cyclicity of the model,  
482 because the dolomitic crust diagenetic facies is present in the subaerial exposure  
483 depositional facies, which are themselves overlain by subtidal depositional facies.  
484 Similarly the high value of the tangent at the origin of transiogram  $t_{d_2e_4}(h)$  shows  
485 that subaerial exposure depositional facies tends to occur above partial dolomite  
486 diagenetic facies, which is also observed in the measured sections (Fig. 10). The  
487 transiograms thus confirm that the method is able to capture asymmetry between

488 depositional and diagenetic facies, so that diagenetic facies are ordered with respect  
489 to the depositional facies.

490 As stated above, the cross-transiograms between depositional facies and diage-  
491 netic facies are not equal to zero for a zero distance. For instance transiogram  $t_{d_1e_4}(h)$   
492 starts at a value close to 1 (Fig. 12) because the dolomitic crust diagenetic facies  $d_1$   
493 is only present in the subaerial exposure diagenetic facies  $e_4$ . The cross-transiogram  
494 then decreases abruptly, which suggests that units of the subaerial exposure dia-  
495 genetic facies are thin, which is consistent with the measured sections (Fig. 10).  
496 Finally, rhythmicity, although not very pronounced, is captured in transiograms  
497  $t_{d_2e_1}(h)$  and  $t_{d_2e_2}(h)$  (Fig. 12). This suggests that partial dolomite diagenetic facies  
498  $d_2$  is separated from subtidal depositional facies  $e_1$  by a nearly constant thickness  
499 of 0.3 m ( $\sim 1$  ft) and that partial dolomite diagenetic facies  $d_2$  is separated from  
500 intertidal depositional facies  $e_2$  by a nearly constant thickness of 1 m ( $\sim 3.3$  ft) (i.e.,  
501 the first maxima of transiograms  $t_{d_2e_1}(h)$  and  $t_{d_2e_2}(h)$ ; Figure 12).

502 The auto- and cross-transiograms of the diagenetic facies themselves are now  
503 fitted using the same procedure. The parameters controlling these transiograms  
504 are the parameters of the third covariance  $r_3$  and  $b_3$  (Eq. A.5), and all the other  
505 parameters mentioned above, which are left unchanged. They control the spatial  
506 properties of  $Z_3$  and thus the geometries of diagenetic facies. Figure 13 shows the fit  
507 between experimental and theoretical transiograms. The method is able to capture  
508 the asymmetry of cross-transiograms between the two diagenetic facies as  $t_{d_2d_1}(h)$   
509 and  $t_{d_1d_2}(h)$ , showing that the dolomitic crust diagenetic facies  $d_1$  tends to overlie  
510 the partial dolomite diagenetic facies  $d_2$ , and the modeled transiograms are able to  
511 match exactly this behavior at the origin (Fig. 13). Theoretical auto-transiograms  
512  $t_{d_1d_1}(h)$  and  $t_{d_2d_2}(h)$  also exhibit the correct behavior at the origin, which confirms  
513 that the mean thicknesses of these diagenetic facies are well constrained (Fig. 13).

514 This section has shown the value of the method for capturing complex tran-  
515 siograms between depositional facies and diagenetic facies. Shifts  $\alpha_{13}$  and  $\alpha_{23}$  play  
516 an important role, which emphasizes the value of incorporating asymmetry in the

517 modeling of syn-depositional diagenetic patterns.

## 518 **Simulation**

519 The simulation is performed as for previously described models (e.g., Figure 8),  
520 with the added third Gaussian random function. Two realizations of the Earth  
521 model showing diagenetic facies superimposed on depositional facies are shown in  
522 Figure 14b and c. Both realizations honor the data along the measured sections  
523 (e.g., long measured section N22; Figure 14b and c), but differ away from them  
524 (e.g., in the volume above measured section N22; Figure 14b and c).

525 To verify that the resulting simulations honor the data statistics, transiograms  
526 are computed on three realizations (thin grey curves in Figure 12 and Figure 13).  
527 The simulated transiograms match the experimental transiograms quite well, even  
528 better than the theoretical transiograms. For instance, transiograms  $t_{d_2e_2}(h)$  for the  
529 realizations reproduce the complex hole-effect observed in the data (Fig. 12). Sim-  
530 ilarly, transiogram  $t_{d_2d_2}(h)$  of the realizations follows the experimental transiogram  
531 more closely than the theoretical transiogram (Fig. 13). This could be due to the  
532 conditioning of the simulation, which provides significant constraints on the Earth  
533 models.

## 534 **Modeling syn-depositional diagenesis in non-stationary shallow-** 535 **marine deposits, Book Cliffs, Utah**

536 The Upper Cretaceous Spring Canyon Member of the Blackhawk Formation, which  
537 is exposed in the Book Cliffs (Utah), consists of shallow-marine, wave-dominated  
538 shoreface sandstones that contain overprinting diagenetic features such as carbonate-  
539 cemented concretions and leached zones (whitecaps) (Van Wagoner et al., 1990;  
540 Kamola and Huntoon, 1995; Hampson and Storms, 2003; Taylor et al., 2004). Due  
541 to their large lateral extent, the deposits display non-stationary facies proportions  
542 from proximal to distal positions. Herein the outcrop dataset is modeled to show the  
543 flexibility of the method and highlight the use of embedded transition probabilities

544 in a non-stationary context.

## 545 **Dataset**

546 The nine measured sections reported by [Taylor et al. \(2004\)](#) are used here, and the  
547 facies classification is simplified into three depositional facies: distal lower shoreface  
548 heteroliths and offshore mudstones ( $E_1$ ), proximal lower shoreface sandstones ( $E_2$ )  
549 and foreshore and upper shoreface sandstones ( $E_3$ ). There are also two diagenetic  
550 facies: carbonate cement  $D_1$  and leached sandstones ("whitecaps")  $D_2$ , in which  
551 carbonate material has been removed via syn-depositional diagenesis. Table 2 shows  
552 the proportion of each diagenetic facies within the different depositional facies, based  
553 on measured sections with this facies classification (Fig. 15).

554 No cyclicity is observed between depositional facies. Facies proportions in each  
555 measured section (represented by pie charts in Figure 15) show that from west  
556 (proximal) to east (distal), the proportion of depositional facies  $E_3$  decreases while  
557 that of depositional facies  $E_1$  increases. Vertical facies proportion curves show that  
558 depositional facies  $E_3$  is only present at the top of the Spring Canyon Member in the  
559 area sampled by the measured sections. Diagenetic facies are also non-stationary  
560 because their distribution is controlled by the distribution of depositional facies  
561 (Table 2).

## 562 **Modeling Non-Stationary Facies Proportions**

563 As described above, facies proportions vary systematically over the dataset to be  
564 modeled (Fig. 15). Therefore, the final Earth model should account for these vari-  
565 ations. This is achieved by estimating the proportions of each facies in each cell of  
566 the Earth model ([Armstrong et al., 2011](#); [D'Or et al., 2017](#)). First, the proportions  
567 of each facies are computed at each horizontal level from all the measured sections  
568 to give vertical facies proportion curves (Fig. 15). The vertical proportion curves are  
569 then smoothed with a moving average algorithm to remove random variations, as  
570 described in [White et al. \(2003\)](#). Then, the proportions of each facies are computed

571 at each vertical measured section (pie charts of Figure 15). Finally, at each grid  
572 cell intersecting a measured section, the proportion of each facies is calculated by  
573 averaging the proportion given by the vertical proportion curve with the proportion  
574 of the facies at the measured section.

575 A procedure to interpolate these facies proportions between measured sections is  
576 then required. Here this is achieved by lateral simple kriging interpolation (Chiles  
577 and Delfiner, 2012) using a Gaussian covariance with a large scale factor and a  
578 mean chosen as the global proportion of each facies. Once the proportions of each  
579 facies have been calculated for every cell of the model, they are transformed into  
580 thresholds for the Gaussian random functions according to the same procedure used  
581 for the models presented earlier (Appendix, Eq. A.8).

## 582 **The Model**

583 The truncation rule can be inferred from the observation of facies contacts in the  
584 measured sections (Fig. 15). Because of the facies distribution's non-stationarity,  
585 the truncation rule is different in every cell and depends on the cell's facies pro-  
586 portion. Therefore, a general truncation rule is first defined in Figure 16, which is  
587 then adapted to the local facies proportions in the different cells of the Earth model  
588 (Fig. 16). The foreshore and upper shoreface sandstone depositional facies ( $E_3$ ) and  
589 distal lower shoreface heteroliths and offshore mudstone depositional facies ( $E_1$ ) are  
590 not in contact, because of a limited presence of foreshore and upper shoreface sand-  
591 stones (which occur only five times in the measured sections) and non stationarity  
592 (Fig. 15). However, there is no reason why these facies should not be in contact  
593 away from the measured sections, and the global truncation rule is thus defined to  
594 allow this contact relationship (Fig. 16). The carbonate cement diagenetic facies  
595 ( $D_1$ ) and leached sandstone diagenetic facies ( $D_2$ ) are respectively present in the  
596 proximal lower shoreface sandstone depositional facies ( $E_2$ ) and both the proximal  
597 lower shoreface sandstone depositional facies and the foreshore and upper shoreface  
598 sandstone depositional facies ( $E_2, E_3$ ) (Fig. 16).

599 Transiograms are not fitted here because their behavior is strongly influenced  
600 by non stationarity, especially at long distances (Armstrong et al., 2011). However,  
601 embedded transition probabilities (Krumbein and Dacey, 1969) are not much af-  
602 fected by non stationarity because they just measure facies juxtapositions. They  
603 can be deduced from the parameters of the model by taking the derivative at the  
604 origin of the transiograms (Eq. A.13). Thus, they are compared to the experimen-  
605 tal embedded transitions computed from the measured sections in order to infer the  
606 parameters  $\alpha_{12}$  and  $\beta_{12}$ . The experimental (red) and model (blue) embedded matrix  
607 for the three depositional facies after fitting is

$$R_{logs/model} = \begin{bmatrix} E_1 & E_2 & E_3 \\ 0 & 1.0/0.63 & 0.0/0.36 \\ 0.72/0.79 & 0 & 0.28/0.23 \\ 0.0/0.15 & 1.0/0.85 & 0 \end{bmatrix}. \quad (1)$$

608 The matrix shows that foreshore and upper shoreface sandstones ( $E_3$ ) and distal  
609 lower shoreface heteroliths and offshore mudstones ( $E_1$ ) are not in contact in the  
610 measured sections because their embedded probability is zero, while in the model  
611 they can be in contact ( $r_{31}=0.15$ ,  $r_{13} = 0.36$ ) according to the truncation rule  
612 (Fig. 16). The embedded transitions from proximal lower shoreface sandstones ( $E_2$ )  
613 to the other depositional facies are similar in the model and in the measured sections.

614 In order to constrain the vertical component of the scale factors  $r_1$  and  $r_2$ , the  
615 thicknesses of the depositional facies are computed in the measured sections and  
616 matched with the theoretical thicknesses, which are obtained from the derivative at  
617 the origin of the auto-transiograms (Carle and Fogg, 1996). The resulting theoretical  
618 thicknesses for the three depositional facies  $E_1$ ,  $E_2$ , and  $E_3$  are respectively 1.3 m  
619 ( $\sim 4.3$  ft), 0.8 m ( $\sim 2.6$  ft), and 0.5 m ( $\sim 1.6$  ft), while the experimental thicknesses  
620 computed from the measured sections are 1.4 m ( $\sim 4.6$  ft), 0.8 m ( $\sim 2.6$  ft), and 0.6  
621 m ( $\sim 2$  ft), which is a good match.

622 Embedded transition probabilities between the diagenetic facies are not shown

623 because they are simply not in contact with each other. The vertical scale factor  $r_3$  is  
624 chosen to be similar to  $r_1$  and  $r_2$  because diagenetic facies have a similar thickness to  
625 depositional facies. Lateral components of the scale factors  $r_1$ ,  $r_2$  and  $r_3$  are chosen  
626 by visual comparison of the resulting Earth model realizations and the correlation  
627 panel between measured sections of Taylor et al. (2004). The depositional facies  
628 have a large lateral extent, of the same order as the west-to-east lateral extent of  
629 the Earth model.

### 630 Simulation

631 The number of cells in the grid in each direction is 100 (west-to-east), 20 (north-to-  
632 south), 566 (height) and the dimensions of the grid are 20 km ( $\sim$ 12.4 mi) (west-to-  
633 east), 5 km ( $\sim$ 3.1 mi) (north-to-south), 56 m ( $\sim$ 184 ft) (height). The simulations  
634 are conditioned to the measured sections with the procedure outlined in Le Blévec  
635 et al. (2018).

636 The original cross section and two realizations of the resulting Earth model  
637 are shown in Figure 17. It is clear that the realizations are non-stationary as, for  
638 instance, the proportion of foreshore and upper shoreface sandstone depositional  
639 facies ( $E_3$ ) decreases towards the west. Leached sandstone diagenetic facies ( $D_2$ )  
640 also exhibit a decreasing proportion towards the west, because they are constrained  
641 by the presence of foreshore and upper shoreface sandstone depositional facies ( $E_3$ )  
642 (Table 2).

643 As a post-validation step, embedded transition probabilities are computed in  
644 three resulting realizations and averaged, to give the embedded matrix of transition  
645 probabilities

$$R_{simu} = \begin{bmatrix} E_1 & E_2 & E_3 \\ 0 & 0.75 & 0.25 \\ 0.79 & 0 & 0.21 \\ 0.06 & 0.94 & 0 \end{bmatrix}. \quad (2)$$

646 This matrix matches the embedded matrix computed from the measured sections



647 (Eq. 1), although foreshore and upper shoreface sandstone depositional facies ( $E_3$ )  
648 and distal lower shoreface heteroliths and offshore mudstone depositional facies ( $E_1$ )  
649 are in contact, as discussed above.

## 650 Discussion

651 The method developed here proposes to model cyclicity and rhythmicity of depo-  
652 sitional facies, combined with diagenesis. This is in itself more than what other  
653 geostatistical methods have offered so far. It appears difficult to model such pat-  
654 terns with sequential indicator simulations (Alabert, 1989) or object-based methods  
655 (Deutsch and Tran, 2002) due to their limitations at modelling inter-facies relation-  
656 ships, while it would be difficult to create a three dimensional training image with  
657 such patterns for inferring multi-point statistics (Strebelle, 2002). The method of  
658 Renard et al. (2008) is a first step forward in the modelling of diagenesis, but their  
659 model is not asymmetric and does not incorporate cyclicity. Therefore, the method  
660 presented here greatly enhances capabilities of geostatistics at building more real-  
661 istic facies Earth models and thus predicting recoverable resources in hydrocarbon  
662 reservoirs.

663 This method could be applied in many other geologic contexts than the ones  
664 presented here. For instance, diagenesis that conforms to facies and bedding patterns  
665 has been modeled here in the Latemar carbonate platform but the method would  
666 also be able to model non-conformable diagenesis. Such diagenesis is sometimes  
667 present in the context of hydrothermal fluid circulation (Davies and Smith Jr, 2006;  
668 Smith Jr, 2006; Vandeginste et al., 2013; Jacquemyn et al., 2014; Beckert et al.,  
669 2015), which tends to create diagenetic structures that follow fractures and faults.  
670 In that case, the third Gaussian function representing diagenesis could be chosen  
671 independent from the Gaussian random functions representing depositional facies,  
672 which would create diagenetic facies cross-cutting depositional facies. Moreover,  
673 the vertical range for this third Gaussian function could be chosen higher than its  
674 lateral range, which would create vertical diagenetic features, as observed along

675 faults. Such a model could be applied to the Latemar carbonate platform, which  
676 shows hydrothermal dolomites along sub-vertical faults and fractures ([Jacquemyn](#)  
677 [et al., 2014](#)).

678 Some limitations of the method should also be noted. Although transiograms  
679 are more informative than variograms thanks to their ability to quantify asymmetry  
680 ([Carle and Fogg, 1996](#)) and thus cyclicity, the cyclicity quantified here is such that  
681 each facies appears only once per cycle. More complex cycles such as symmetric cy-  
682 cles (a fining-upward sequence overlying a coarsening-upward sequence, for example)  
683 cannot be quantified by two-point statistics such as transiograms. More complex  
684 cycles could possibly be quantified with higher order statistics, which could be used  
685 to infer the method developed here. Moreover, the experimental transiograms in the  
686 case studies of this paper are not perfectly fitted by the method. More work could  
687 be carried out on developing covariance models with more complex hole-effects in  
688 order to better capture rhythmicity in some datasets. Further development of the  
689 truncation rule would also give more flexibility to fit all the transition rates between  
690 facies.

## 691 **Conclusion and Recommendations**

692 The new method proposed in this paper models depositional and diagenetic facies  
693 fields with cyclic and rhythmic patterns. The method is based on a novel Pluri-  
694 Gaussian approach, using three dimensional truncation rules and Gaussian random  
695 functions shifted from each other. Qualitative information and concepts are used to  
696 construct the truncation rule, and the other parameters of the method are defined by  
697 fitting the experimental auto- and cross- transiograms. The resulting models show  
698 that a combination of lateral and vertical facies cyclicity can be used to generate  
699 aggradational and progradational facies geometries.

700 In addition, the method models depositional facies overprinted by conformable  
701 diagenesis. This is possible because the three Gaussian random functions are spa-  
702 tially shifted from each other, and depositional and diagenetic facies are ordered

703 according to the cross-transiograms.

704 The method has also shown its capability to model non-stationary facies propor-  
705 tions, which is a predominant feature in datasets that contain pronounced proximal-  
706 to-distal or axial-to-marginal facies trends. In such cases, it is not appropriate to  
707 use transiograms to constrain the parameters of the method. Instead, it is sug-  
708 gested to use embedded transition probabilities, because non stationarity does not  
709 significantly impact facies juxtapositions.

710 The method significantly improves the capability of geostatistical Earth models  
711 to represent geologically realistic facies architectures, and thus can lead to more  
712 realistic geostatistical reservoir models and more accurate hydrocarbon production  
713 forecasts. The source code of this method is hosted on Github and freely available  
714 at <https://github.com/tleblevecIMP/CyclicPGS>.

## 715 A Appendix: Shifted Pluri-Gaussian Model

716 The model developed in this paper is an extension of that developed by [Le Blévec](#)  
717 [et al. \(2018\)](#). Three Gaussian random functions  $Z_1, Z_2, Z_3$  are correlated and shifted  
718 relative to each other and truncated into facies according to a truncation rule (e.g.,  
719 [Figure 11](#)). The first two Gaussian random functions control depositional facies while  
720 the third Gaussian random function controls diagenetic facies. A shifted version of  
721 the linear model of co-regionalization ([Wackernagel, 2003](#)) is used

$$\begin{cases} Z_1(x) = Y_1(x), \\ Z_2(x) = \beta_{12} Y_1(x + \alpha_{12}) + \sqrt{1 - \beta_{12}^2} Y_2(x), \\ Z_3(x) = \beta_{13} Y_1(x + \alpha_{13}) + \beta_{23} Y_2(x + \alpha_{23}) + \sqrt{1 - \beta_{13}^2 - \beta_{23}^2} Y_3(x), \end{cases} \quad (\text{A.3})$$

722 where  $-1 < \beta_{ij} < 1$  are the correlations coefficients between  $Y_i(x + \alpha_{ij})$  and  $Z_j(x)$ ,  
723  $\alpha_{ij}$  being the shifts, and  $Y_1, Y_2, Y_3$  are uncorrelated Gaussian random functions with

724 respective covariances in three dimensions

$$\rho_1(h_x, h_y, h_z) = \exp\left(-\frac{h_x^2}{r_{1x}^2} - \frac{h_y^2}{r_{1y}^2} - \frac{h_z^2}{r_{1z}^2}\right) \cos(b_1 h_z), \quad (\text{A.4a})$$

725

$$\rho_2(h_x, h_y, h_z) = \exp\left(-\frac{h_x^2}{r_{2x}^2} - \frac{h_y^2}{r_{2y}^2} - \frac{h_z^2}{r_{2z}^2}\right) \cos(b_2 h_z), \quad (\text{A.4b})$$

726

$$\rho_3(h_x, h_y, h_z) = \exp\left(-\frac{h_x^2}{r_{3x}^2} - \frac{h_y^2}{r_{3y}^2} - \frac{h_z^2}{r_{3z}^2}\right) \cos(b_3 h_z), \quad (\text{A.4c})$$

727 with  $r_i = (r_{ix}, r_{iy}, r_{iz})$  the scale factors in three dimensions and  $b_i$  the frequencies of  
 728 the cosine functions. Therefore, the auto-covariances of the three Gaussian random  
 729 functions  $Z_1, Z_2, Z_3$  are respectively

$$\begin{cases} \rho_{Z_1}(h) = \rho_1(h), \\ \rho_{Z_2}(h) = \beta_{12}^2 \rho_1(h) + (1 - \beta_{12}^2) \rho_2(h), \\ \rho_{Z_3}(h) = \beta_{13}^2 \rho_1(h) + \beta_{23}^2 \rho_2(h) + (1 - \beta_{13}^2 - \beta_{23}^2) \rho_3(h), \end{cases} \quad (\text{A.5})$$

730 and the cross-covariances between them

$$\begin{cases} \rho_{Z_1 Z_2}(h) = \beta_{12} \rho_1(h + \alpha_{12}), \\ \rho_{Z_1 Z_3}(h) = \beta_{13} \rho_1(h + \alpha_{13}), \\ \rho_{Z_2 Z_3}(h) = \beta_{12} \beta_{13} \rho_1(h + \alpha_{13} - \alpha_{12}) + \beta_{23} \sqrt{1 - \beta_{12}^2} \rho_2(h + \alpha_{23}). \end{cases} \quad (\text{A.6})$$

731 These covariances are used to derive the thresholds of the Gaussian random functions  
 732 from the proportions of the different facies. For instance, let us determine the  
 733 threshold  $q_{d_1}$  of the third Gaussian random function  $Z_1$  that controls the proportion  
 734 of facies  $d_1$  (Fig. 11)

$$p_{d_1} = Pr[Z_1(x) > q_1, Z_2(x) < q_3, Z_3(x) > q_{d_1}], \quad (\text{A.7})$$

735 which can be re-written by integration of the multi-variate Gaussian density  $G_{\Sigma}(u, v, w)$

$$p_{d1} = \int_{q_1}^{\infty} \int_{-\infty}^{q_2} \int_{q_{d1}}^{\infty} G_{\Sigma}(u, v, w) du dv dw, \quad (\text{A.8})$$

736 with  $\Sigma$  the covariance matrix

$$\Sigma = \begin{bmatrix} 1 & \rho_{Z_1 Z_2}(0) & \rho_{Z_1 Z_3}(0) \\ \rho_{Z_1 Z_2}(0) & 1 & \rho_{Z_2 Z_3}(0) \\ \rho_{Z_1 Z_3}(0) & \rho_{Z_2 Z_3}(0) & 1 \end{bmatrix}. \quad (\text{A.9})$$

737 Equation A.8 is then solved numerically with the algorithm of Genz (1992). The  
738 same methodology is applied to compute theoretical transiograms (Fig. 7). For  
739 instance, let us examine the transiogram between facies  $e_1$  and  $e_2$  (Fig. 11)

$$t_{e_1 e_2}(h) = \frac{Pr[Z_1(x) < q_1, Z_2(x) < q_2, Z_1(x+h) < q_1, Z_2(x+h) > q_2]}{p_{e_1}}, \quad (\text{A.10})$$

740 which can be re-written by integration of Gaussian multi-variate density

$$t_{e_1 e_2}(h) = \frac{1}{p_{e_1}} \int_{-\infty}^{q_1} \int_{-\infty}^{q_2} \int_{-\infty}^{q_1} \int_{q_2}^{\infty} G_{\Sigma(h)}(u, v, w, y) du dv dw dy, \quad (\text{A.11})$$

741 with  $\Sigma(h)$  the covariance matrix

$$\Sigma(h) = \begin{bmatrix} 1 & \rho_{Z_1 Z_2}(0) & \rho_{Z_1}(h) & \rho_{Z_1 Z_2}(h) \\ \rho_{Z_1 Z_2}(0) & 1 & \rho_{Z_2 Z_1}(h) & \rho_{Z_2}(h) \\ \rho_{Z_1}(h) & \rho_{Z_2 Z_1}(h) & 1 & \rho_{Z_1 Z_2}(0) \\ \rho_{Z_1 Z_2}(h) & \rho_{Z_2}(h) & \rho_{Z_1 Z_2}(0) & 1 \end{bmatrix}. \quad (\text{A.12})$$

742 Equation A.11 is then solved numerically with the algorithm of Genz (1992) and the  
743 same methodology is applied for the other transiograms. The embedded transition  
744 probabilities are computed numerically from the transiograms as follows

$$r_{ij} = -\frac{t'_{ij}(0)}{t'_{ii}(0)}. \quad (\text{A.13})$$

## 746 **References**

747 Alabert F (1989) Non-Gaussian data expansion in the earth sciences. *Terra Nova*  
748 1(2):123–134

749 Alabert F, Modot V (1992) Stochastic models of reservoir heterogeneity: Impact on  
750 connectivity and average permeabilities. In: SPE Annual Technical Conference  
751 and Exhibition, 4-7 October, Washington, D.C, Society of Petroleum Engineers

752 Armstrong M, Galli A, Beucher H, Loc'h G, Renard D, Doligez B, Eschard R, Geffroy  
753 F (2011) *PluriGaussian simulations in geosciences*. Berlin, Springer Science &  
754 Business Media

755 Barbier M, Hamon Y, Doligez B, Callot JP, Floquet M, Daniel JM (2012) Stochastic  
756 joint simulation of facies and diagenesis: a case study on early diagenesis of the  
757 Madison formation (Wyoming, USA). *Oil & Gas Science and Technology–Revue*  
758 *d'IFP Energies nouvelles* 67(1):123–145

759 Bartok P, Reijers T, Juhasz I (1981) Lower Cretaceous Cogollo Group, Maracaibo  
760 Basin, Venezuela: sedimentology, diagenesis, and petrophysics. *AAPG Bulletin*  
761 65(6):1110–1134

762 Beckert J, Vandeginste V, John CM (2015) Exploring the geological features and  
763 processes that control the shape and internal fabrics of late diagenetic dolomite  
764 bodies (Lower Khuff equivalent–Central Oman Mountains). *Marine and Petroleum*  
765 *Geology* 68:325–340

766 Burgess P, Wright V, Emery D (2001) Numerical forward modelling of peritidal car-  
767 bonate parasequence development: implications for outcrop interpretation. *Basin*  
768 *Research* 13(1):1–16

- 769 Burgess PM (2016) Identifying ordered strata: Evidence, methods, and meaning.  
770 *Journal of Sedimentary Research* 86(3):148–167
- 771 Carle SF, Fogg GE (1996) Transition probability-based indicator geostatistics. *Math-*  
772 *ematical geology* 28(4):453–476
- 773 Carle SF, Fogg GE (1997) Modeling spatial variability with one and multidimen-  
774 sional continuous-lag markov chains. *Mathematical Geology* 29(7):891–918
- 775 Carrera MFL, Barbier M, Le Ravalec M (2018) Accounting for diagenesis overprint in  
776 carbonate reservoirs using parametrization technique and optimization workflow  
777 for production data matching. *Journal of Petroleum Exploration and Production*  
778 *Technology* pp 1–15
- 779 Chiles JP, Delfiner P (2012) *Geostatistics: modeling spatial uncertainty*. Hoboken,  
780 John Wiley & Sons
- 781 Cisne JL (1986) Earthquakes recorded stratigraphically on carbonate platforms.  
782 *Nature* 323(6086):320
- 783 Davies GR, Smith Jr LB (2006) Structurally controlled hydrothermal dolomite reser-  
784 voir facies: An overview. *AAPG bulletin* 90(11):1641–1690
- 785 De Boer P, Wonders A (1984) Astronomically induced rhythmic bedding in Creta-  
786 ceous pelagic sediments near Moria (Italy). *Milankovitch and climate* pp 177–190
- 787 Deutsch C, Tran T (2002) Fluvsim: a program for object-based stochastic modeling  
788 of fluvial depositional systems. *Computers & Geosciences* 28(4):525–535
- 789 Doligez B, Hamon Y, Barbier M, Nader F, Lerat O, Beucher H (2011) Advanced  
790 workflows for joint modelling of sedimentary facies and diagenetic overprint, im-  
791 pact on reservoir quality. *Proceedings - SPE Annual Technical Conference and*  
792 *Exhibition*, 3 pp 2003–2016

- 793 D'Or D, David E, Walgenwitz A, Pluyaud P, Allard D (2017) Non stationary pluri-  
794 Gaussian simulations with auto-adaptative truncation diagrams using the cart  
795 algorithm. In: 79th EAGE Conference and Exhibition 2017
- 796 Dubrule O (2017) Indicator variogram models: Do we have much choice? *Mathe-*  
797 *matical Geosciences* 49(4):441–465
- 798 Egenhoff SO, Peterhänsel A, Bechstädt T, Zühlke R, Grötsch J (1999) Facies ar-  
799 chitecture of an isolated carbonate platform: tracing the cycles of the Latemar  
800 (Middle Triassic, northern Italy). *Sedimentology* 46(5):893–912
- 801 Fabricius IL, Røgen B, Gommesen L (2007) How depositional texture and diagenesis  
802 control petrophysical and elastic properties of samples from five north sea chalk  
803 fields. *Petroleum Geoscience* 13(1):81–95
- 804 Genz A (1992) Numerical computation of multivariate normal probabilities. *Journal*  
805 *of computational and graphical statistics* 1(2):141–149
- 806 Gingerich PD (1969) Markov analysis of cyclic alluvial sediments. *Journal of sedi-*  
807 *mentary research* 39(1)
- 808 Ginsburg RN (1957) Early diagenesis and lithification of shallow-water carbonate  
809 sediments in south Florida. *Special Publications of SEPM* 5
- 810 Goldhammer R, Dunn P, Hardie L (1990) Depositional cycles, composite sea-level  
811 changes, cycle stacking patterns, and the hierarchy of stratigraphic forcing: ex-  
812 amples from Alpine Triassic platform carbonates. *Geological Society of America*  
813 *Bulletin* 102(5):535–562
- 814 Goldhammer R, Lehmann P, Dunn P (1993) The origin of high-frequency platform  
815 carbonate cycles and third-order sequences (Lower Ordovician El Paso Gp, west  
816 Texas): constraints from outcrop data and stratigraphic modeling. *Journal of*  
817 *Sedimentary Research* 63(3)



- 818 Grotzinger JP (1986) Evolution of Early Proterozoic passive-margin carbonate plat-  
819 form, rocknest formation, wopmay orogen, Northwest Territories, Canada. *Journal*  
820 *of Sedimentary Research* 56(6)
- 821 Hampson GJ, Storms JE (2003) Geomorphological and sequence stratigraphic  
822 variability in wave-dominated, shoreface-shelf parasequences. *Sedimentology*  
823 50(4):667–701
- 824 Hattori I (1976) Entropy in Markov chains and discrimination of cyclic patterns in  
825 lithologic successions. *Journal of the International Association for Mathematical*  
826 *Geology* 8(4):477–497
- 827 Hinnov LA, Goldhammer RK (1991) Spectral analysis of the Middle Triassic  
828 Latemar limestone. *Journal of Sedimentary Research* 61(7):1173–1193
- 829 House MR (1985) A new approach to an absolute timescale from measurements of  
830 orbital cycles and sedimentary microrhythms. *Nature* 315(6022):721
- 831 Jacquemyn C, El Desouky H, Hunt D, Casini G, Swennen R (2014) Dolomitization of  
832 the Latemar platform: Fluid flow and dolomite evolution. *Marine and Petroleum*  
833 *Geology* 55:43–67
- 834 Jones TA, Ma YZ (2001) Teacher's aide: geologic characteristics of hole-effect  
835 variograms calculated from lithology-indicator variables. *Mathematical Geology*  
836 33(5):615–629
- 837 Jordan Jr CF (1973) Carbonate facies and sedimentation of patch reefs off Bermuda.  
838 *AAPG Bulletin* 57(1):42–54
- 839 Kamola DL, Huntoon JE (1995) Repetitive stratal patterns in a foreland basin  
840 sandstone and their possible tectonic significance. *Geology* 23(2):177–180
- 841 Koltermann CE, Gorelick SM (1996) Heterogeneity in sedimentary deposits: A re-  
842 view of structure-imitating, process-imitating, and descriptive approaches. *Water*  
843 *Resources Research* 32(9):2617–2658

- 844 Krumbein WC, Dacey MF (1969) Markov chains and embedded Markov chains  
845 in geology. *Journal of the International Association for Mathematical Geology*  
846 1(1):79–96
- 847 Le Blévec T, Dubrule O, John CM, Hampson GJ (2017) Modelling asymmetrical fa-  
848 cies successions using pluri-Gaussian simulations. In: *Geostatistics Valencia 2016*,  
849 Springer, pp 59–75
- 850 Le Blévec T, Dubrule O, John CM, Hampson GJ (2018) Geostatistical modelling of  
851 cyclic and rhythmic facies architectures. *Mathematical Geosciences* URL <https://doi.org/10.1007/s11004-018-9737-y>  
852
- 853 Lindsay RF, Cantrell DL, Hughes GW, Keith TH, Mueller III HW, Russell SD  
854 (2006) Ghawar Arab-D reservoir: widespread porosity in shoaling-upward car-  
855 bonate cycles, Saudi Arabia. *AAPG Special Volumes*
- 856 Madani N, Emery X (2015) Simulation of geo-domains accounting for chronology  
857 and contact relationships: application to the río blanco copper deposit. *Stochastic*  
858 *environmental research and risk assessment* 29(8):2173–2191
- 859 Makhloufi Y, Collin PY, Bergerat F, Casteleyn L, Claes S, David C, Menendez B,  
860 Monna F, Robion P, Sizun JP, et al. (2013) Impact of sedimentology and diagenesis  
861 on the petrophysical properties of a tight oolitic carbonate reservoir. the case of  
862 the Oolithe Blanche Formation (Bathonian, Paris Basin, France). *Marine and*  
863 *Petroleum Geology* 48:323–340
- 864 Matheron G, Beucher H, de Fouquet C, Galli A, Ravenne C (1988) Simulation  
865 conditionnelle à trois faciès dans une falaise de la formation du Brent. *Sciences de*  
866 *la Terre, Série Informatique Géologique* 28:213–249
- 867 Middleton GV (1973) Johannes Walther’s law of the correlation of facies. *Geological*  
868 *Society of America Bulletin* 84(3):979–988
- 869 Moore CH, Wade WJ (2013) Carbonate reservoirs: Porosity and diagenesis in a  
870 sequence stratigraphic framework, vol 67. Amsterdam, Elsevier

- 871 Peterhänsel A, Egenhoff SO (2008) Lateral variabilities of cycle stacking patterns in  
872 the Latemar, Triassic, Italian Dolomites. *SEPM Spec Publ* 89:217–229
- 873 Pontiggia M, Ortenzi A, Ruvo L, et al. (2010) New integrated approach for diagen-  
874 esis characterization and simulation. In: *North Africa Technical Conference and*  
875 *Exhibition, Society of Petroleum Engineers*
- 876 Pyrcz MJ, Deutsch CV (2014) *Geostatistical reservoir modeling*. Oxford, Oxford  
877 university press
- 878 Rameil N (2008) Early diagenetic dolomitization and dedolomitization of Late Juras-  
879 sic and earliest Cretaceous platform carbonates: a case study from the Jura Moun-  
880 tains (NW Switzerland, E France). *Sedimentary Geology* 212(1-4):70–85
- 881 Renard D, Beucher H, Doligez B (2008) Heterotopic bi-categorical variables in pluri-  
882 Gaussian truncated simulations. In: *Proceedings of the Eighth International Geo-*  
883 *statistics Congress Geostats*, pp 289–298
- 884 Sharp I, Gillespie P, Morsalnezhad D, Taberner C, Karpuz R, Vergés J, Horbury  
885 A, Pickard N, Garland J, Hunt D (2010) Stratigraphic architecture and fracture-  
886 controlled dolomitization of the Cretaceous Khami and Bangestan groups: an  
887 outcrop case study, Zagros Mountains, Iran. *Geological Society, London, Special*  
888 *Publications* 329(1):343–396
- 889 Smith Jr LB (2006) Origin and reservoir characteristics of upper Ordovician  
890 Trenton–Black River hydrothermal dolomite reservoirs in New York. *AAPG bul-*  
891 *letin* 90(11):1691–1718
- 892 Strasser A (1988) Shallowing-upward sequences in Purbeckian peritidal carbon-  
893 ates (lowermost Cretaceous, Swiss and French Jura Mountains). *Sedimentology*  
894 35(3):369–383
- 895 Strebelle S (2002) Conditional simulation of complex geological structures using  
896 multiple-point statistics. *Mathematical Geology* 34(1):1–21

- 897 Taylor KG, Gawthorpe RL, Fannon-Howell S (2004) Basin-scale diagenetic alter-  
898 ation of shoreface sandstones in the Upper Cretaceous Spring Canyon and Ab-  
899 erdeen Members, Blackhawk Formation, Book Cliffs, Utah. *Sedimentary Geology*  
900 172(1-2):99–115
- 901 Taylor TR, Giles MR, Hathon LA, Diggs TN, Braunsdorf NR, Birbiglia GV, Kit-  
902 tridge MG, Macaulay CI, Espejo IS (2010) Sandstone diagenesis and reservoir  
903 quality prediction: Models, myths, and reality. *AAPG bulletin* 94(8):1093–1132
- 904 Van Wagoner JC, Mitchum R, Campion K, Rahmanian V (1990) Siliciclastic se-  
905 quence stratigraphy in well logs, cores, and outcrops: concepts for high-resolution  
906 correlation of time and facies. *AAPG methods in exploration series*, 0743-0531 ;  
907 no 7
- 908 Vandeginste V, John CM, van de Flierdt T, Cosgrove JW (2013) Linking process,  
909 dimension, texture, and geochemistry in dolomite geobodies: A case study from  
910 Wadi Mistal (northern Oman) linking process, dimension, texture, and geochem-  
911 istry in dolomite geobodies. *AAPG bulletin* 97(7):1181–1207
- 912 Verrill AE (1907) The Bermuda islands. part 4, geology and paleontology. *Trans*  
913 *Connecticut Academy Arts Sciences* 12:316
- 914 Wackernagel H (2003) *Multivariate geostatistics: an introduction with applications*.  
915 Berlin, Springer Science & Business Media
- 916 Wang L, Wong P, Shibli S, et al. (1998) Modelling porosity distribution in the a’nan  
917 oilfield: Use of geological quantification, neural networks and geostatistics. In:  
918 *SPE International Oil and Gas Conference and Exhibition in China*, Society of  
919 *Petroleum Engineers*
- 920 White CD, Novakovic D, Dutton SP, Willis BJ (2003) A geostatistical model for  
921 calcite concretions in sandstone. *Mathematical Geology* 35(5):549–575
- 922 Wilkinson BH, Drummond CN, Rothman ED, Diedrich NW (1997) Stratal order in  
923 peritidal carbonate sequences. *Journal of Sedimentary research* 67(6):1068–1082

## 924 Table and Figure Captions

925 Table 1: Proportions of diagenetic facies overprinted on depositional facies in the  
926 Latemar carbonate platform, taken from measured sections (Fig. 10).

927 Table 2: Proportions of diagenetic facies overprinted on depositional facies in the  
928 Spring Canyon Member of the Blackhawk Formation, taken from measured sections  
929 (Fig. 15).

930 Figure 1: Four synthetic facies successions: (a) cyclic and rhythmic; (b) non  
931 rhythmic with two cycles; (c) rhythmic (blue facies) with two cycles; and (d) cyclic  
932 and non rhythmic. Modified from [Le Blévec et al. \(2018\)](#).

933 Figure 2: Cyclic and rhythmic facies succession (a) with associated transiogram  
934 matrix between facies 1 and 2 (b-e).  $\overline{L}_c$  is the mean thickness of a facies cycle, and  
935  $\overline{L}_1$  and  $\overline{L}_2$  are the mean thicknesses of facies 1 and 2. Proportion of facies 1 is 0.5  
936 and proportion of facies 2 is 0.25.

937 Figure 3: Facies succession (a) modeled with Truncated Gaussian Simulations ac-  
938 cording to the truncation rule (b) and parameters  $r_1 = 0.1$  m ( $\sim 0.3$  ft),  $(p_1, p_2, p_3) =$   
939  $(0.4, 0.4, 0.2)$  (Eq. [A.4a](#)).

940 Figure 4: Comparison between conventional Pluri-Gaussian Simulation (PGS)  
941 (b) and shifted PGS (c) with the same truncation rule (a). For (b), the parameters  
942 are  $r_1 = r_2 = 0.6$  m ( $\sim 2$  ft),  $b_1 = 15$  m<sup>-1</sup> ( $\sim 49$  ft<sup>-1</sup>),  $b_2 = 30$  m<sup>-1</sup> ( $\sim 98$  ft<sup>-1</sup>)  
943 (Eqs. [A.4a](#), [A.4b](#)), and facies proportions  $(p_1, p_2, p_3) = (0.5, 0.25, 0.25)$  and for (c),  
944 the same parameters are applied together with the shift  $\alpha_{12} = 0.04$  m ( $\sim 0.13$  ft)  
945 and correlation coefficient  $\beta_{12} = -0.7$  (Eq. [A.3](#)).

946 Figure 5: Measured sections through part of the Upper Cyclic Facies interval in  
947 the Cimon Latemar outcrop, Latemar platform. Figure modified from [Peterhänsel](#)  
948 [and Egenhoff \(2008\)](#).

949 Figure 6: Truncation rule used for modeling depositional facies in the Latemar  
950 platform dataset (Fig. 5).

951 Figure 7: Experimental transiograms (grey points) in the upward vertical direc-  
952 tion of depositional facies computed from the measured sections shown in Figure 5,

953 theoretical transiograms fitted to these points (black line), and transiograms com-  
 954 puted in three realizations of the depositional facies Earth model (thin grey lines).  
 955 The parameters used for the theoretical transiograms are  $r_1 = (800, 800, 0.3)$  m  
 956 ( $\sim(2624, 2624, 1)$  ft),  $r_2 = (800, 800, 1.2)$  m ( $\sim(2624, 2624, 3.9)$  ft),  $b_2 = 5 \text{ m}^{-1}$  ( $\sim 16$   
 957  $\text{ft}^{-1}$ ),  $\beta_{12} = 0.67$ ,  $\alpha_{12} = 0.1$  m ( $\sim 0.3$  ft) (Eqs. A.4a, A.4b).

958 Figure 8: Cross section interpreted by Peterhänsel and Egenhoff (2008) (a) and  
 959 two realizations of an Earth model for depositional facies (b and c) in the Cimon  
 960 region of the Latemar carbonate platform conditioned by four measured sections  
 961 (Fig. 5) with modeling parameters explained in Figures 7.

962 Figure 9: Three dimensional unconditional realization from a satellite image  
 963 of Bermuda carbonate platform interior. (a) satellite image (with latitudinal and  
 964 longitudinal position) showing three types of facies based on visual interpretation:  
 965 blue represents the lagoon, light green the backreef, and dark green the reef; (b)  
 966 truncation rule; and (c) 3D Earth model of facies distributions. The parameters of  
 967 the simulation are  $r_1 = r_2 = (20, 100, 0.4)$  m ( $\sim(66, 328, 13)$  ft),  $\alpha_{12} = (0.1, 5)$  m  
 968 ( $\sim(0.3, 16)$  ft),  $(p_1, p_2, p_3) = (0.15, 0.15, 0.7)$  (Eqs. A.4a, A.4b).

969 Figure 10: Depositional facies and diagenetic facies in the measured sections  
 970 through part of the Upper Cyclic Facies in Cimon Latemar outcrop, Latemar car-  
 971 bonate platform (Fig. 5). Measured sections are adapted from Peterhänsel and  
 972 Egenhoff (2008).

973 Figure 11: Three dimensional truncation rule used for modeling the depositional  
 974 facies and diagenetic facies in the Latemar platform dataset (Fig. 10, Table 1).

975 Figure 12: Experimental vertical cross-transiograms between depositional facies  
 976 and diagenetic facies (grey points) from measured sections shown in Figure 10, theo-  
 977 retical cross-transiograms fitted to these points (black lines), and cross-transiograms  
 978 computed in three realizations of a resulting Earth model (thin grey lines). The pa-  
 979 rameters defining the theoretical transiograms are the same as those for Figure 7,  
 980 with in addition  $\beta_{13} = -0.8$ ,  $\beta_{23} = -0.5$ ,  $\alpha_{13} = -0.1$  m ( $\sim -0.3$  ft),  $\alpha_{23} = 0.1$  m  
 981 ( $\sim 0.3$  ft) (Eq. A.3).

982 Figure 13: Experimental transiograms between diagenetic facies (grey points),  
983 theoretical transiograms fitted to these points (black lines), and transiograms com-  
984 puted in three realizations of a resulting Earth model (thin grey lines). The param-  
985 eters defining the theoretical transiograms are the same as those for Figure 7 and  
986 12, with in addition  $r_3 = (800, 800, 0.3)$  m ( $\sim(2625, 2625, 1)$  ft) (Eq. A.4c).

987 Figure 14: Cross section interpreted by Peterhänsel and Egenhoff (2008) (a) and  
988 two realisations of an Earth model for depositional facies and diagenetic facies (b,  
989 and c) in the Cimon Latemar region of the Latemar carbonate platform, conditioned  
990 by four measured sections (Fig. 10) with modeling parameters noted in Figure 7, 12  
991 and 13.

992 Figure 15: Measured sections through the Spring Canyon Member, Blackhawk  
993 Formation in outcrops of the Book Cliffs, as reported by Taylor et al. (2004), with  
994 simplified classification of depositional facies and diagenetic facies, corresponding fa-  
995 cies vertical proportion curves, and pie charts of facies proportions in each measured  
996 section.

997 Figure 16: Global truncation rule and two examples of local truncation rules  
998 for modeling the Spring Canyon Member, Blackhawk Formation in outcrops of the  
999 Book Cliffs. The facies E are depositional facies and D are diagenetic facies.

1000 Figure 17: Cross section modified from Taylor et al. (2004) and two realizations  
1001 of an Earth model for depositional facies and diagenetic facies (b and c) in the Spring  
1002 Canyon Member, Blackhawk Formation, conditioned by nine measured sections  
1003 (Fig. 15) with modeling parameters  $r_1 = (0.6, 3000, 3000)$  m ( $\sim(2,9842, 9842)$  ft),  
1004  $r_2 = (0.7, 3000, 3000)$  m ( $\sim(2.3, 9842, 9842)$  ft),  $r_3 = (1, 1500, 1500)$  m ( $\sim(3.3, 4921, 4921)$   
1005 ft),  $\alpha_{12} = \alpha_{13} = \alpha_{23} = 0$  m (0 ft),  $\beta_{12} = \beta_{13} = \beta_{23} = 0$  (Eqs. A.3, A.4a, A.4b, A.4c).

Table 1:

	Dolomitic crust	Partial dolomite
Subtidal	0	0
Intertidal	0	0.10
Supratidal	0	0.02
Exposure	0.32	0

Table 2:

	Carbonate concretion	White caps
Distal mudstones	0	0
Shoreface sandstones	0.21	0.03
Foreshore sandstones	0.59	0.4

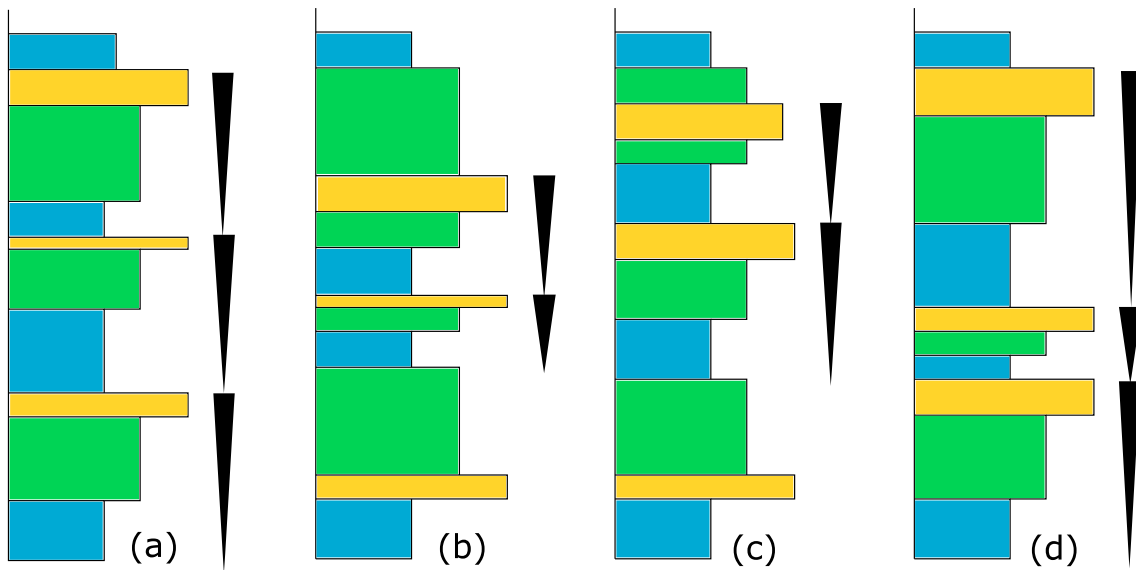


Figure 1:



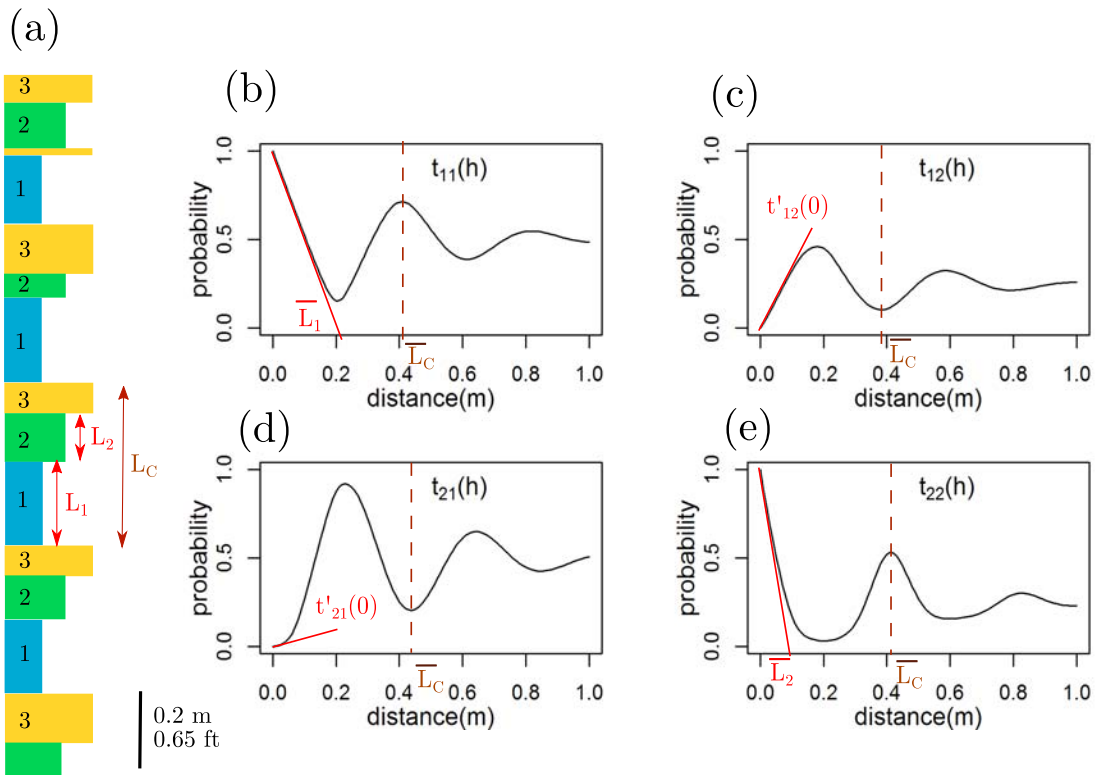


Figure 2:

(a) Truncated Gaussian Simulation

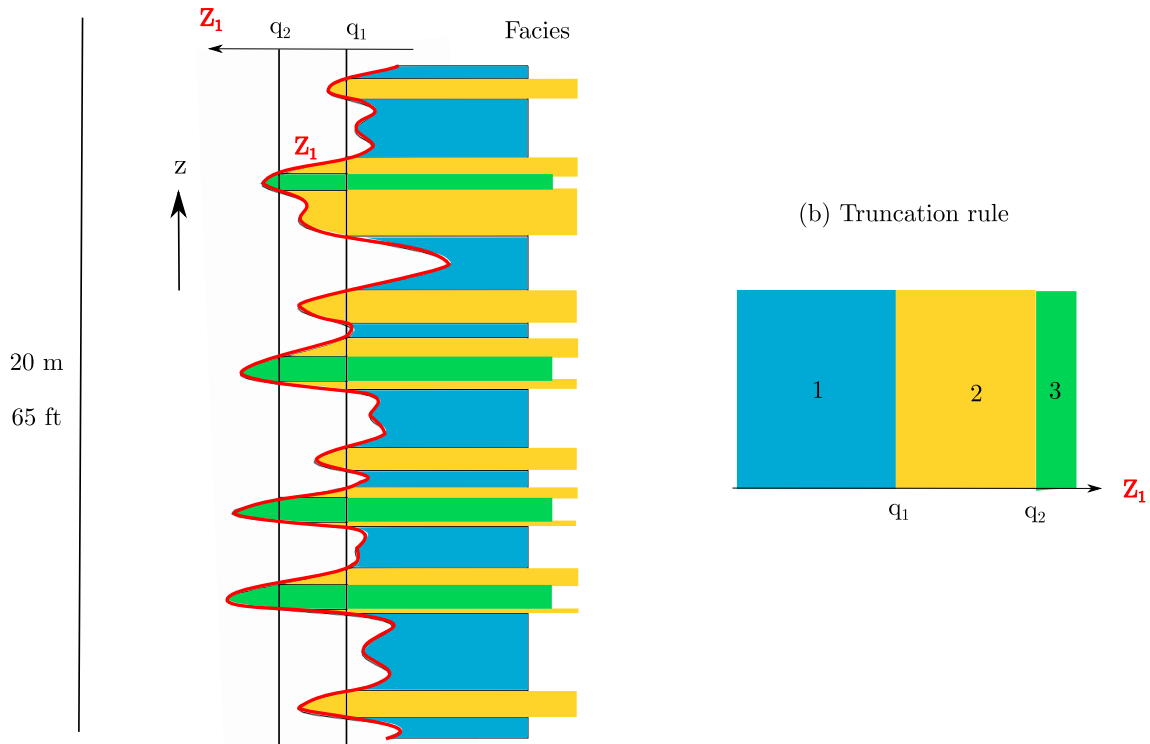


Figure 3:

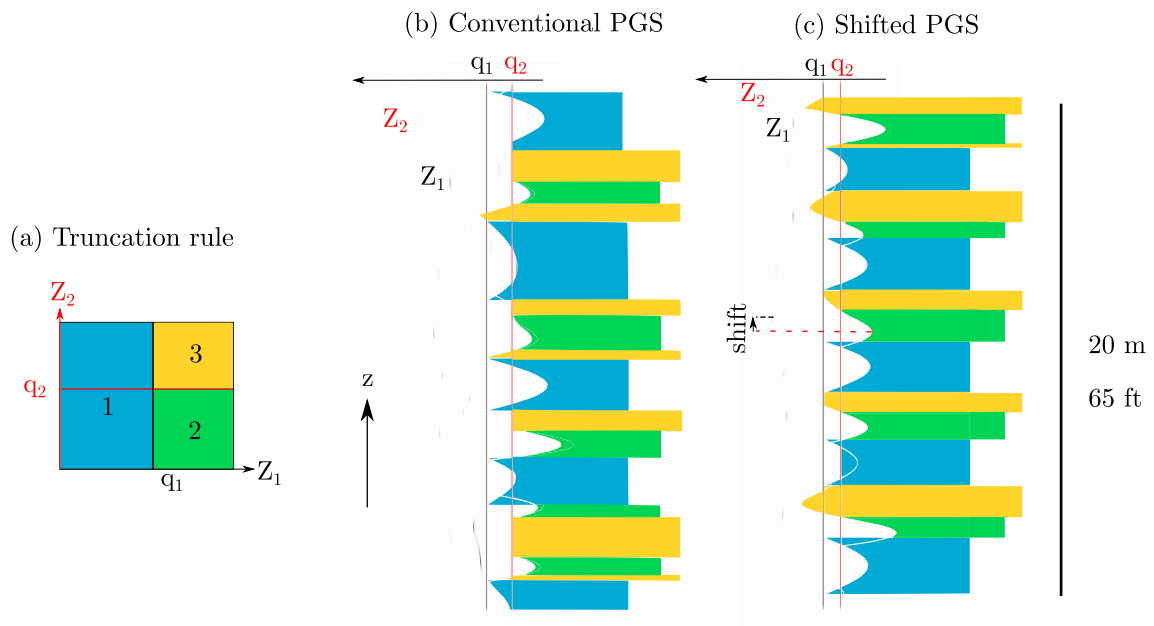


Figure 4:

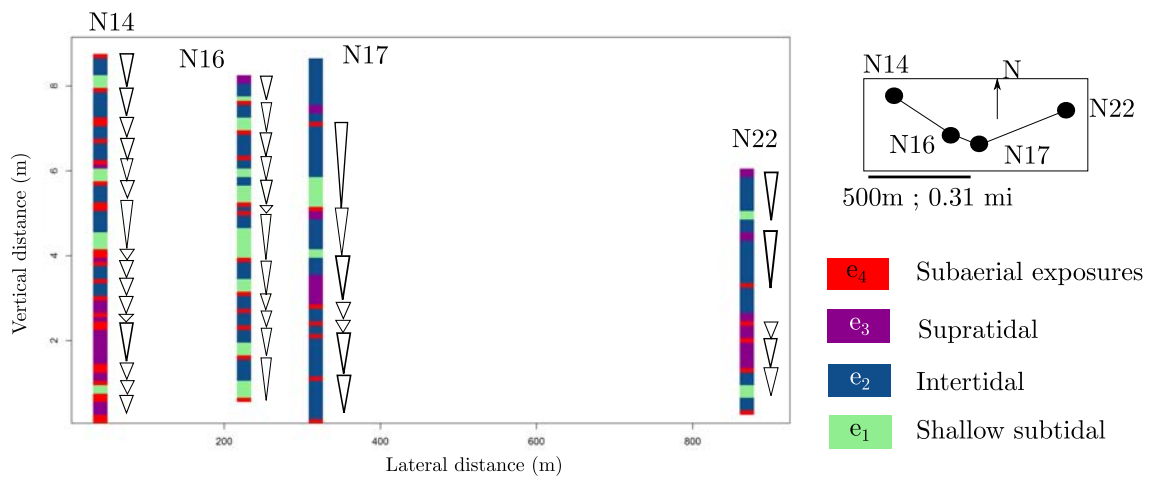


Figure 5:

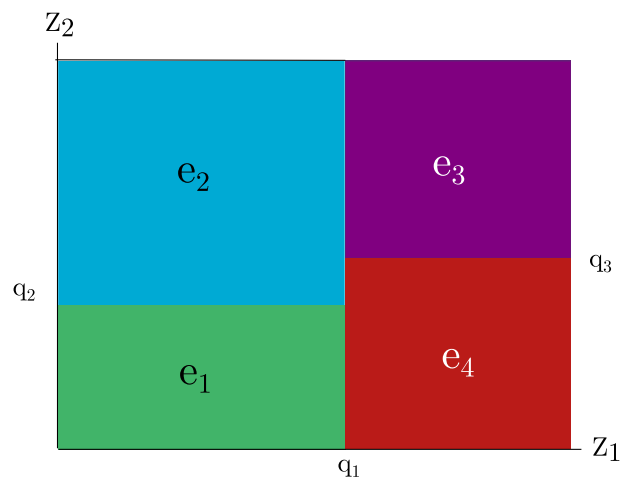


Figure 6:

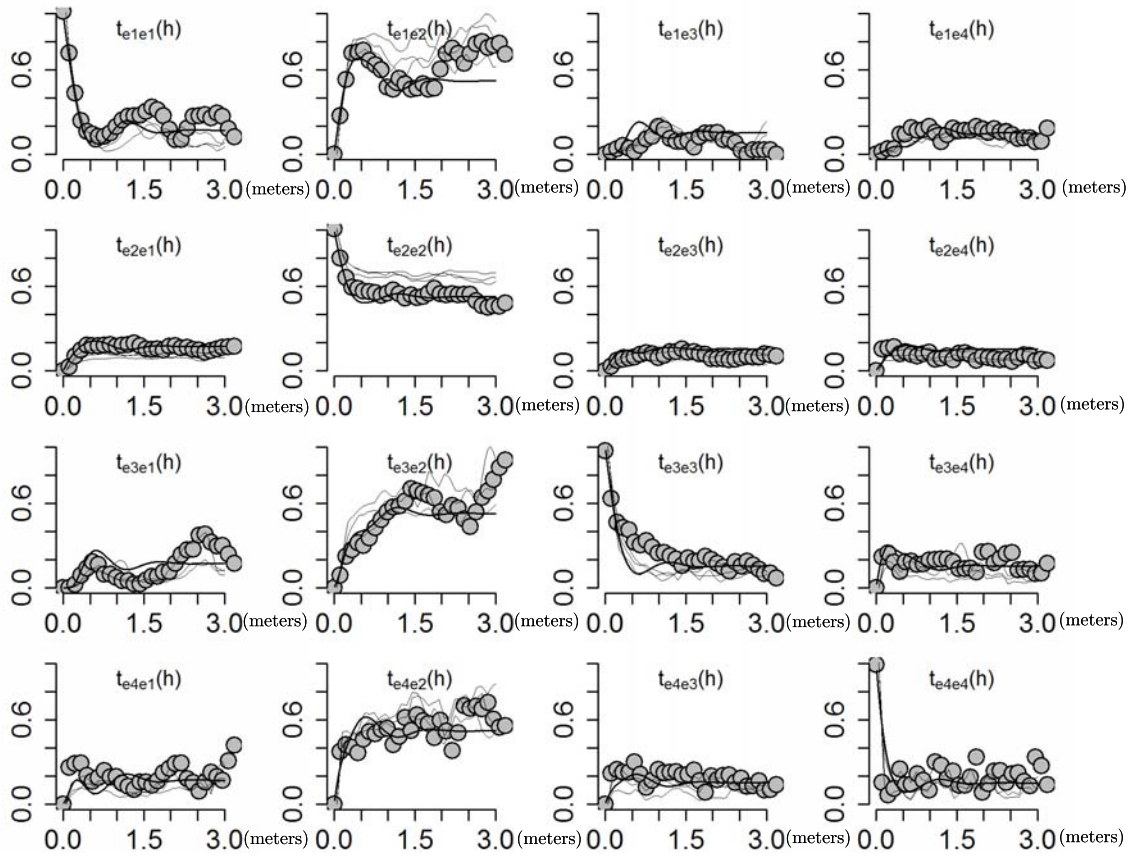


Figure 7:

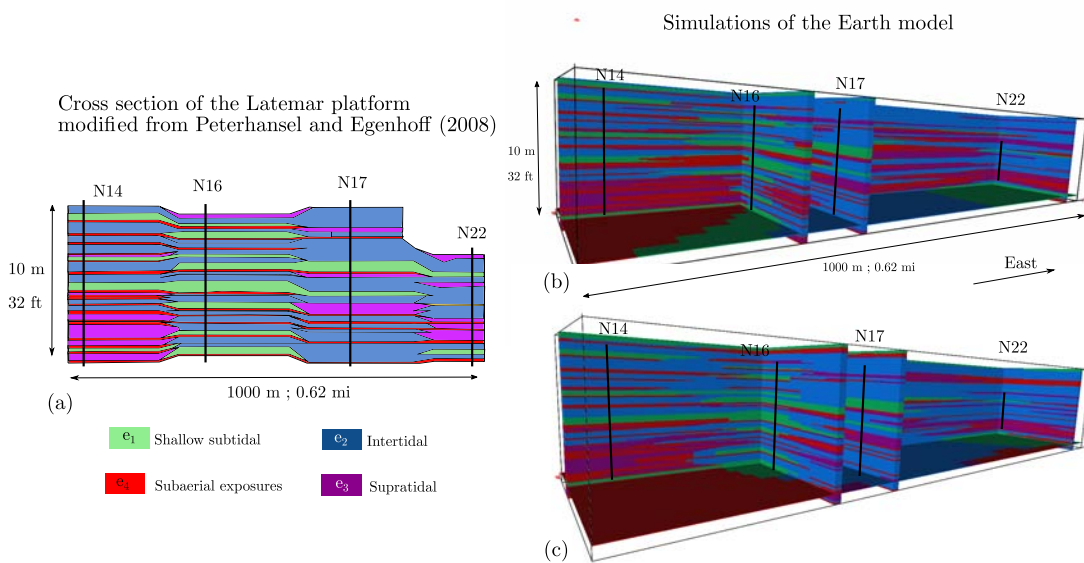
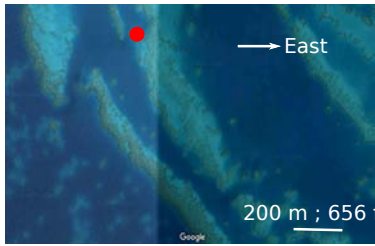


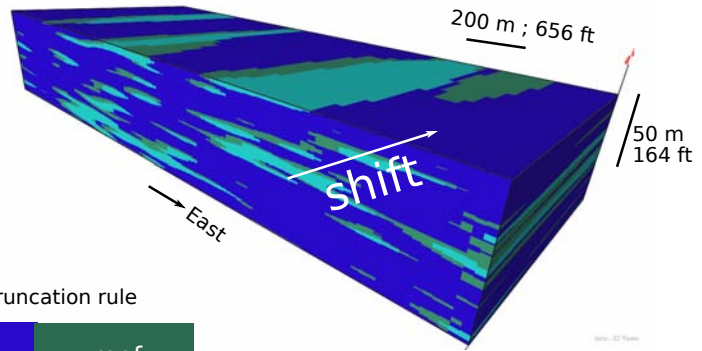
Figure 8:

(a) Shallow carbonates (Bermuda) in map view



● Position: (32.315688, -64.918218)

(c) Three dimensional corresponding simulation with shifted PGS



(b) Truncation rule

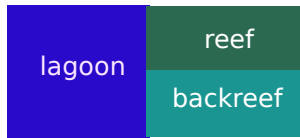


Figure 9:

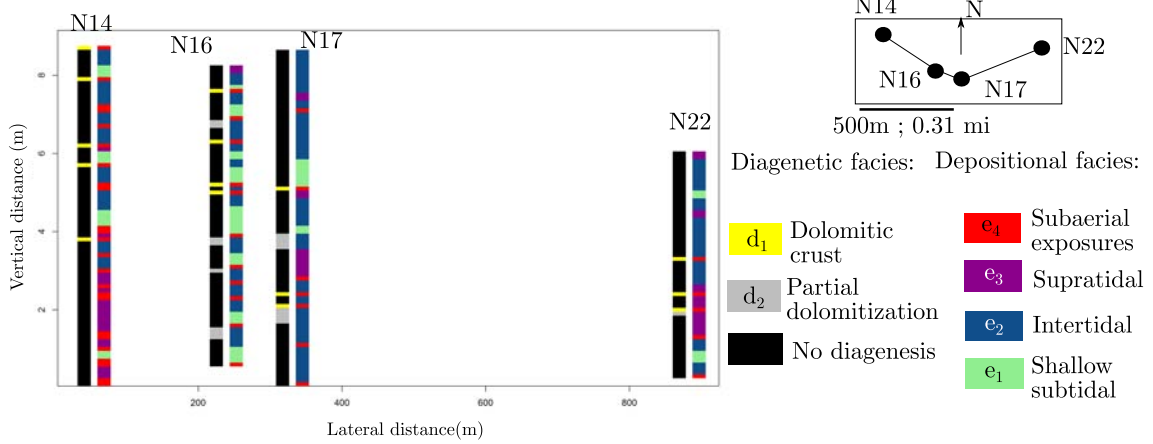


Figure 10:

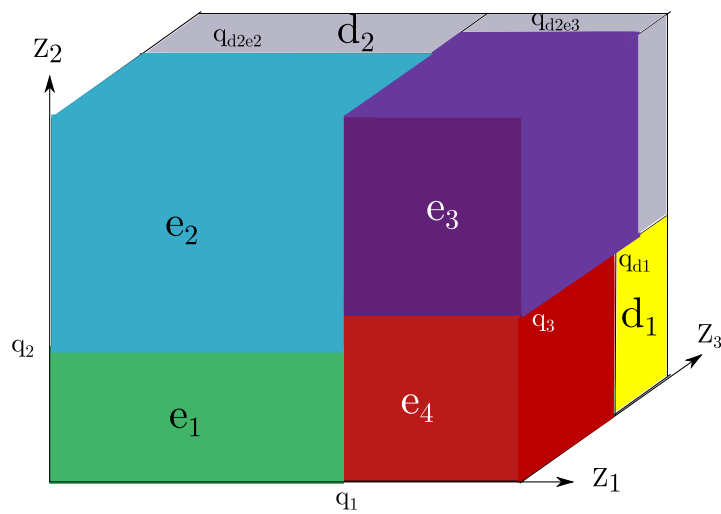


Figure 11:

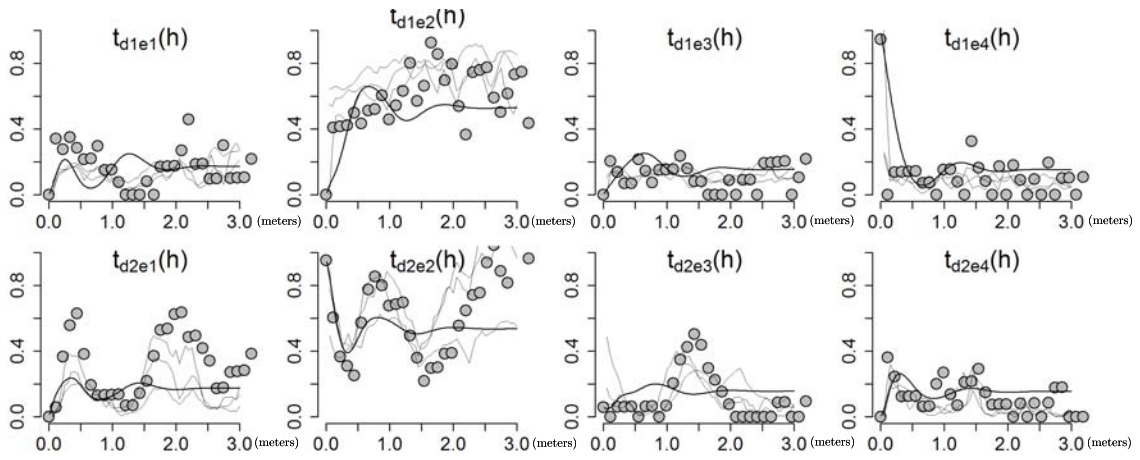


Figure 12:

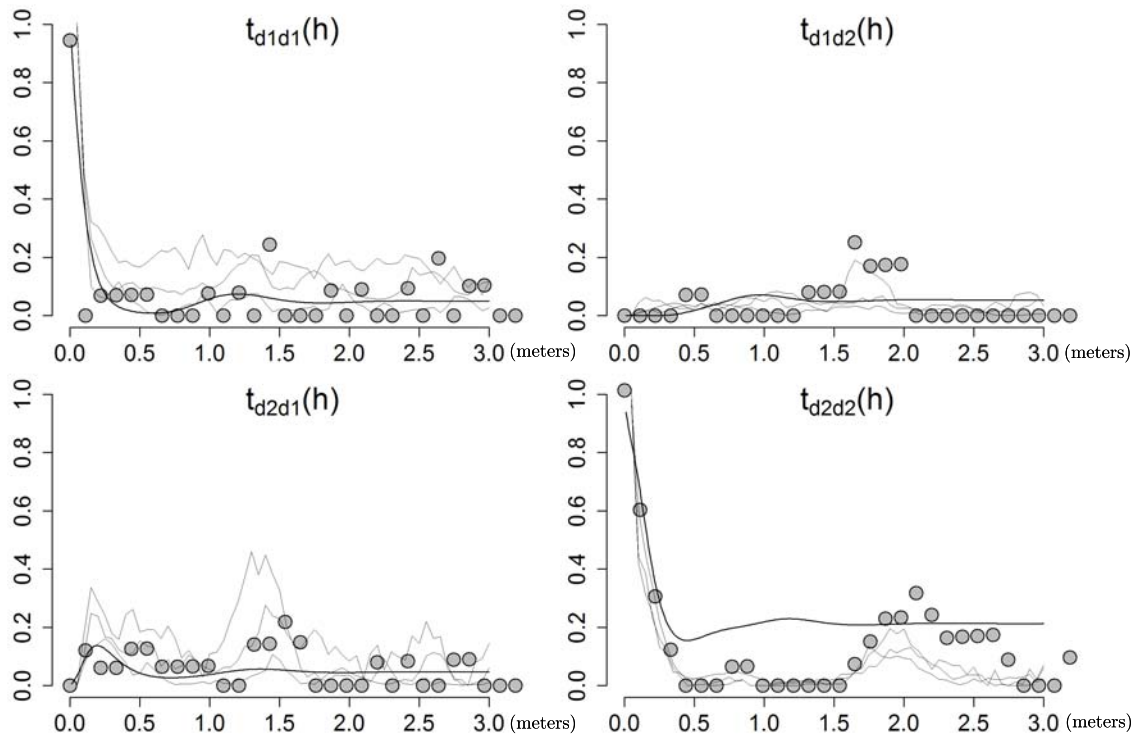


Figure 13:

Simulations of the Earth model

Cross section of the Latemar platform modified from Peterhansel and Egenhoff (2008)

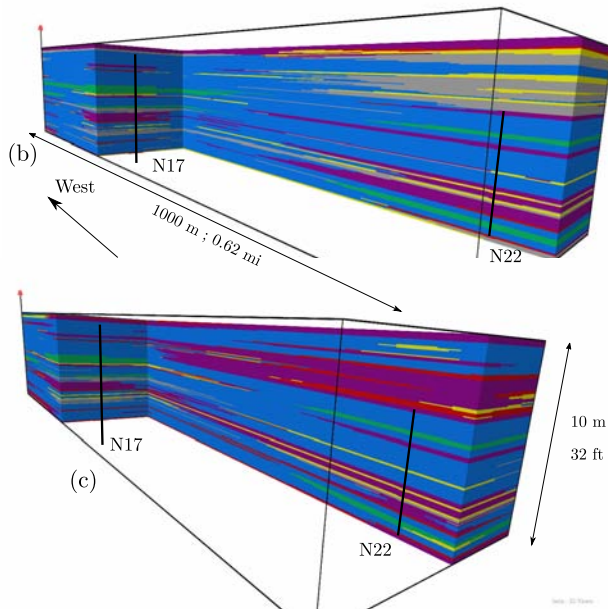
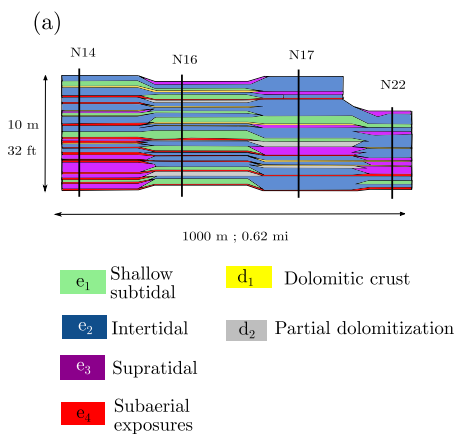


Figure 14:

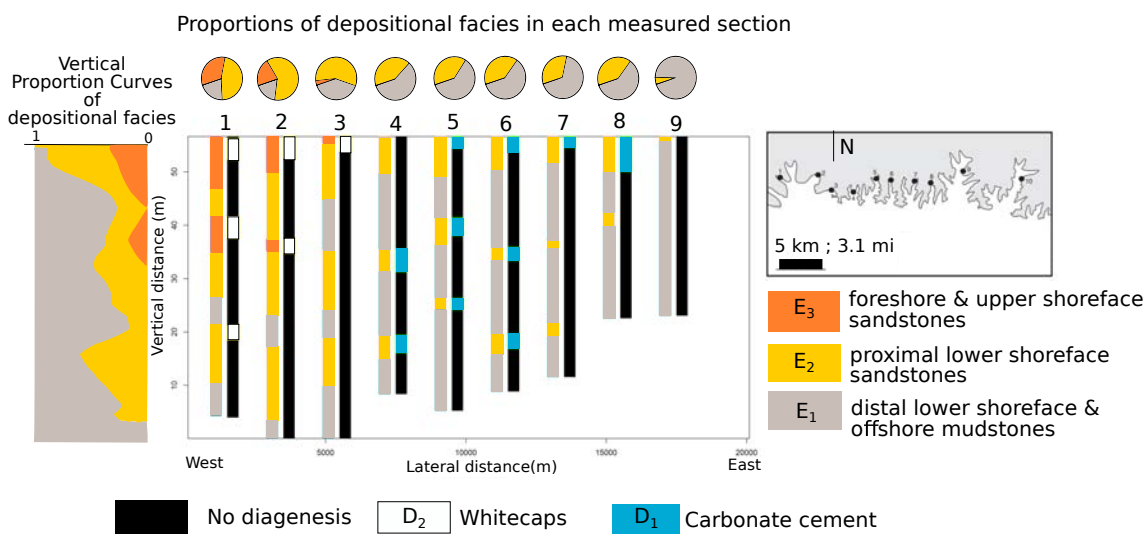


Figure 15:

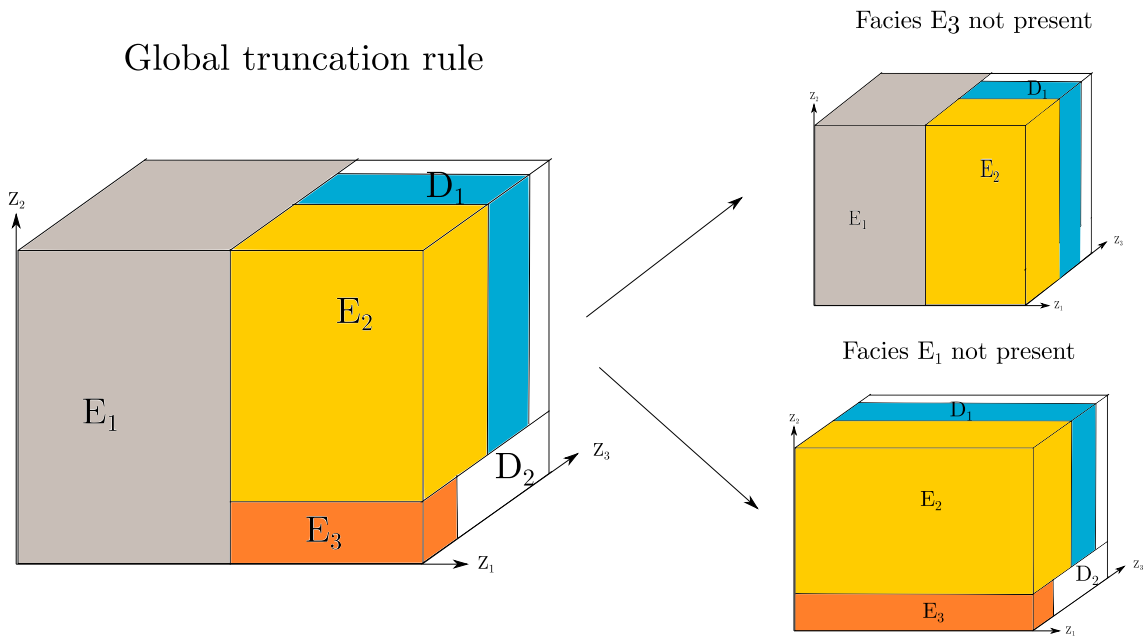


Figure 16:

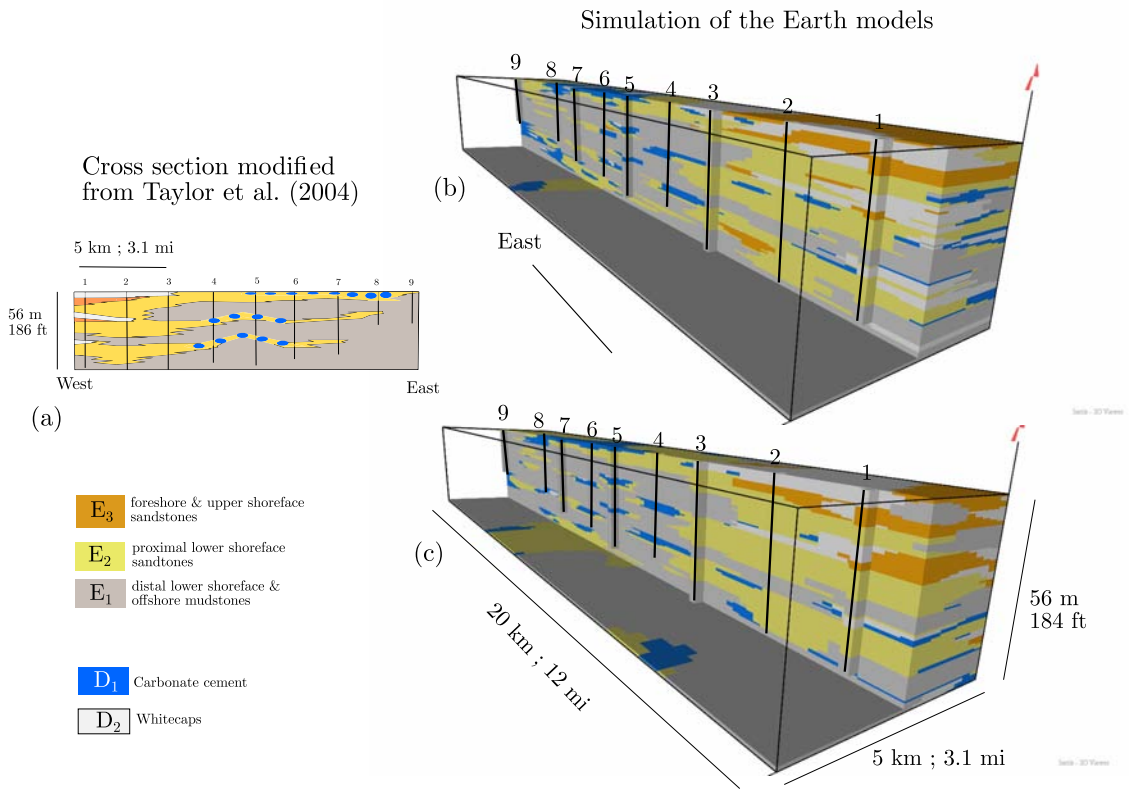


Figure 17: